Pressure anisotropy in global magnetospheric simulations: A magnetohydrodynamics model

X. Meng,[1] G. Tóth,[1] M. W. Liemohn,[1] T. I. Gombosi,[1] and A. Runov[2]

Received 3 April 2012; revised 15 June 2012; accepted 27 June 2012; published 11 August 2012.

[1] In order to better describe the space plasmas where pressure anisotropy has prominent effects, we extend the BATS-R-US magnetohydrodynamics (MHD) model to include anisotropic pressure. We implement the anisotropic MHD equations under the double adiabatic approximation with an additional pressure relaxation term into BATS-R-US and perform global magnetospheric simulations. The results from idealized magnetospheric simulations confirm previous studies: pressure anisotropy widens the magnetosheath, increases the density depletion in the vicinity of the magnetopause, enhances the nightside plasma pressure, and introduces an eastward ring current. In addition, we find that the flow speed in the magnetotail is significantly reduced by including pressure anisotropy in MHD simulations. Our model is validated through comparing the simulations to the THEMIS data on both the dayside and nightside of the magnetosphere during quiet times. The comparison to the results from isotropic MHD simulations implies that although anisotropic MHD is comparable to isotropic MHD in matching the measurement, it improves the simulated plasma velocity in some cases.

Citation: Meng, X., G. Tóth, M. W. Liemohn, T. I. Gombosi, and A. Runov (2012), Pressure anisotropy in global magnetospheric simulations: A magnetohydrodynamics model, *J. Geophys. Res.*, *117*, A08216, doi:10.1029/2012JA017791.

1. Introduction

[2] Pressure anisotropy is important in magnetized plasmas with low densities, where particle collisions are not frequent enough to balance the particle motions along and perpendicular to the magnetic field. Thus the corresponding parallel and perpendicular pressures are different. Space plasmas provide the favored environments where the pressure anisotropy arises. In the Earth's magnetosphere, such environments include the magnetosheath, the tail reconnection region, and the closed-field-line region surrounding the Earth.

[3] To describe the pressure anisotropy feature of space plasmas that cannot be captured by ideal magnetohydrodynamics (MHD) simulations, we extend the BATS-R-US MHD code [*Powell et al.*, 1999] to account for anisotropic pressure. A major difficulty during the implementation is the insufficient jump relations across a discontinuity in an anisotropic plasma [*Abraham-Shrauner*, 1967; *Lynn*, 1967; *Neubauer*, 1970], requiring us to develop special treatments in order to compute the bow shock accurately. In addition, several types of plasma instabilities can arise in an anisotropic plasma [*Chandrasekhar et al.*, 1958; *Barnes*, 1966; *Kennel and Petschek*, 1966], restricting the pressure anisotropy. Finally, we need to perform verification and validation tests to ensure the numerical and physical correctness of the model itself.

[4] Our study is being conducted in several steps. In our recent paper [*Meng et al.*, 2012], we reported in detail the implementation and verification of BATS-R-US with anisotropic pressure. There we described the equations for MHD with anisotropic ion pressure and isotropic electron pressure under both the classical and semirelativistic limits. The ion pressure equations are the same as the double adiabatic equations [*Chew et al.*, 1956] plus an anisotropy relaxation term. We also presented the characteristic wave speeds acquired by numerical fluxes, the numerical algorithm and a set of numerical tests that we performed to verify the anisotropic MHD code. In the present paper, we focus on the Earth's quiet time magnetospheric simulations to validate the anisotropic MHD model. We also investigate the timescale for limiting the pressure anisotropy in the simulations. In a follow-up paper, we will describe the coupling between anisotropic BATS-R-US and ring current models, particularly the Comprehensive Ring Current Model (CRCM) [*Fok et al.*, 2001], which resolves pitch angle distribution and thus can provide pressure anisotropy information in the inner magnetosphere to anisotropic BATS-R-US. The coupled model is used to perform geomagnetic storm simulations. Since the electron pressure plays a minor role compared to the ion pressure in the magnetosphere, we do not consider electron pressure in our magnetospheric modeling.

[5] No global magnetospheric MHD models considering pressure anisotropy have been developed to our knowledge.

[1]Department of Atmospheric, Oceanic and Space Sciences, University of Michigan, Ann Arbor, Michigan, USA.
[2]Institute of Geophysics and Planetary Physics, University of California Los Angeles, Los Angeles, California, USA.

Corresponding author: X. Meng, Center for Space Environment Modeling, University of Michigan, 2455 Hayward St., Ann Arbor, MI 48109, USA. (xingm@umich.edu)

0148-0227/12/2012JA017791

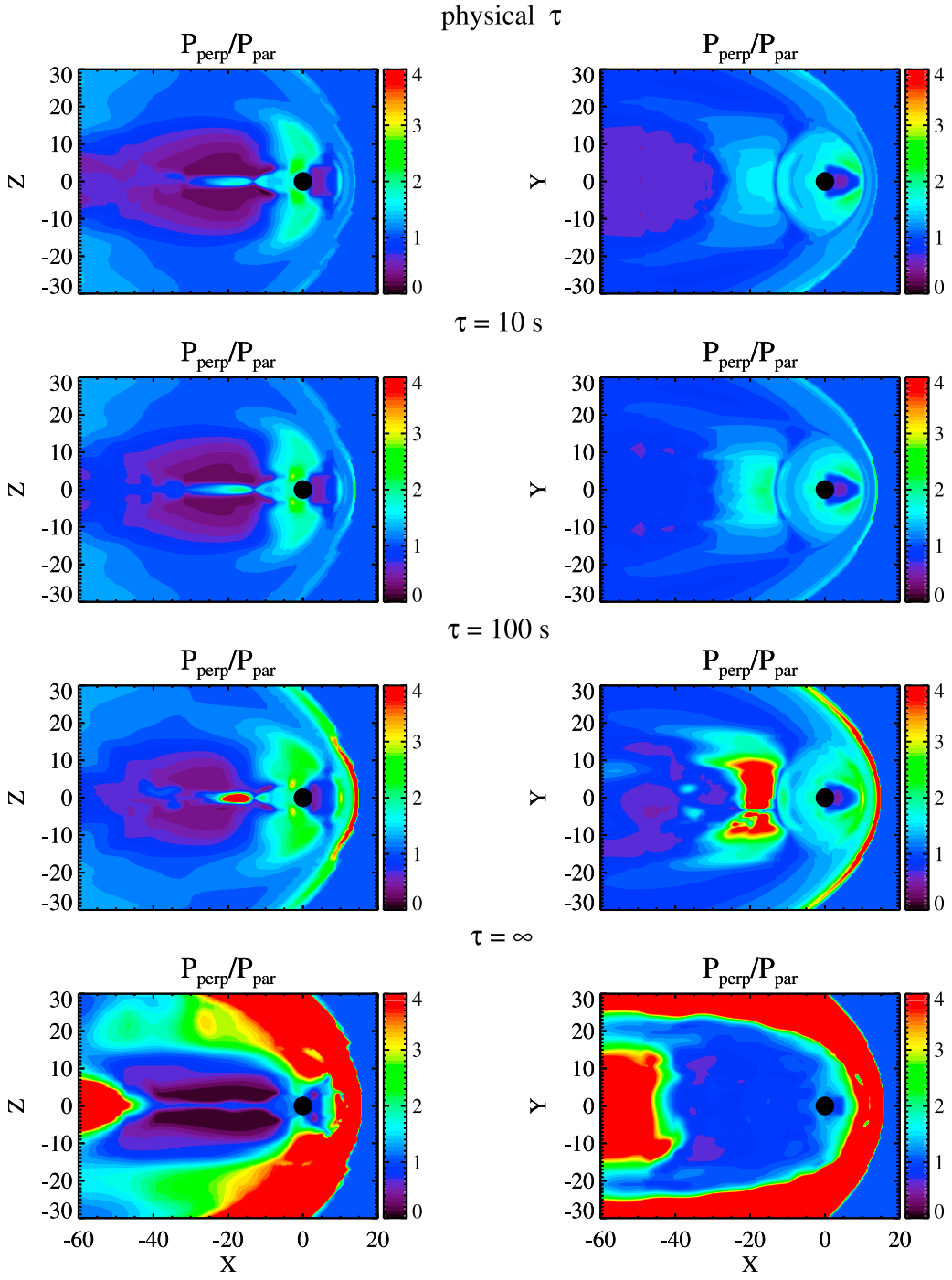

Figure 1. The pressure anisotropy ratio $p_\perp / p_\parallel$ in the $Y = 0$ plane (left column) and the $Z = 0$ plane (right column) from the idealized magnetospheric simulations using anisotropic BATS-R-US in the southward IMF case. The four rows are from runs with different pressure relaxation time τ. Top to bottom: growth-rate based τ, τ = 10 s, τ = 100 s, $\tau = \infty$ (no pressure relaxation).

Nevertheless, MHD modeling with anisotropic pressure has been addressed by many publications. A heavily studied topic is the anisotropic MHD model of the magnetosheath. For example, *Erkaev et al.* [1999] presented a three-dimensional (3-D) steady state MHD model of the magnetosheath flow near the subsolar line with anisotropic pressure. *Denton and Lyon* [2000] studied the effects of pressure anisotropy using a two-dimensional (2-D) fluid model of the magnetosheath. Recently, *Samsonov et al.* [2007] validated their 3-D anisotropic MHD model of the magnetosheath by comparing the model results to Cluster data. The magnetotail has also been simulated with a 3-D anisotropic MHD model

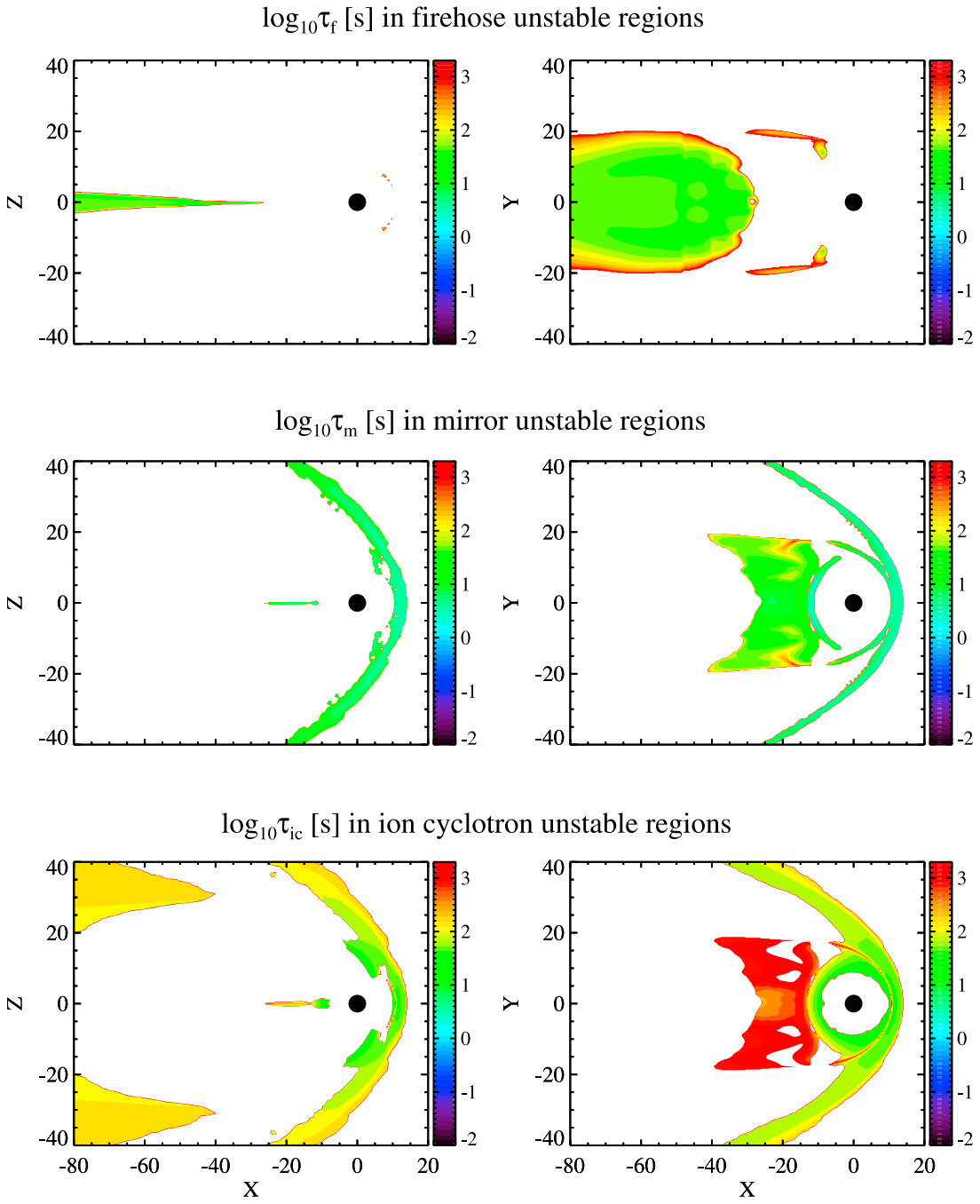

Figure 2. The logarithmic τ contour in the $Y = 0$ plane (left column) and the $Z = 0$ plane (right column) of the three instabilities from the growth-rate based τ run for the southward IMF case. τ is given in seconds. The white regions are stable for the respective instabilities.

by *Hesse and Birn* [1992]. These regional models significantly contribute to the numerical modeling of space plasmas with anisotropic pressure, however they cannot reveal the global impacts of pressure anisotropy.

[6] In addition to the study of MHD models, a few researchers have investigated pressure anisotropy with equilibrium models. *Cheng* [1992] obtained self-consistent magnetospheric equilibria with anisotropic pressure by solving the inverse equilibrium equation. *Zaharia et al.* [2004] computed 3-D force-balanced magnetospheric configurations with their 3-D equilibrium code and applied to magnetic storm simulations. *Wu et al.* [2009] extended a friction code equilibrium solver to include pressure anisotropy. These studies provide very interesting insight of how anisotropic pressures modify the magnetic field and current configuration in the inner magnetosphere. Yet the equilibrium modeling, relying on empirical models of the pressure distribution as initial inputs, is very different from the self-consistent and time-dependent MHD model presented in this paper.

[7] Moverover, pressure anisotropy has been studied with empirical models, which belong to another important branch of magnetospheric modeling techniques. *Horton et al.* [1993]

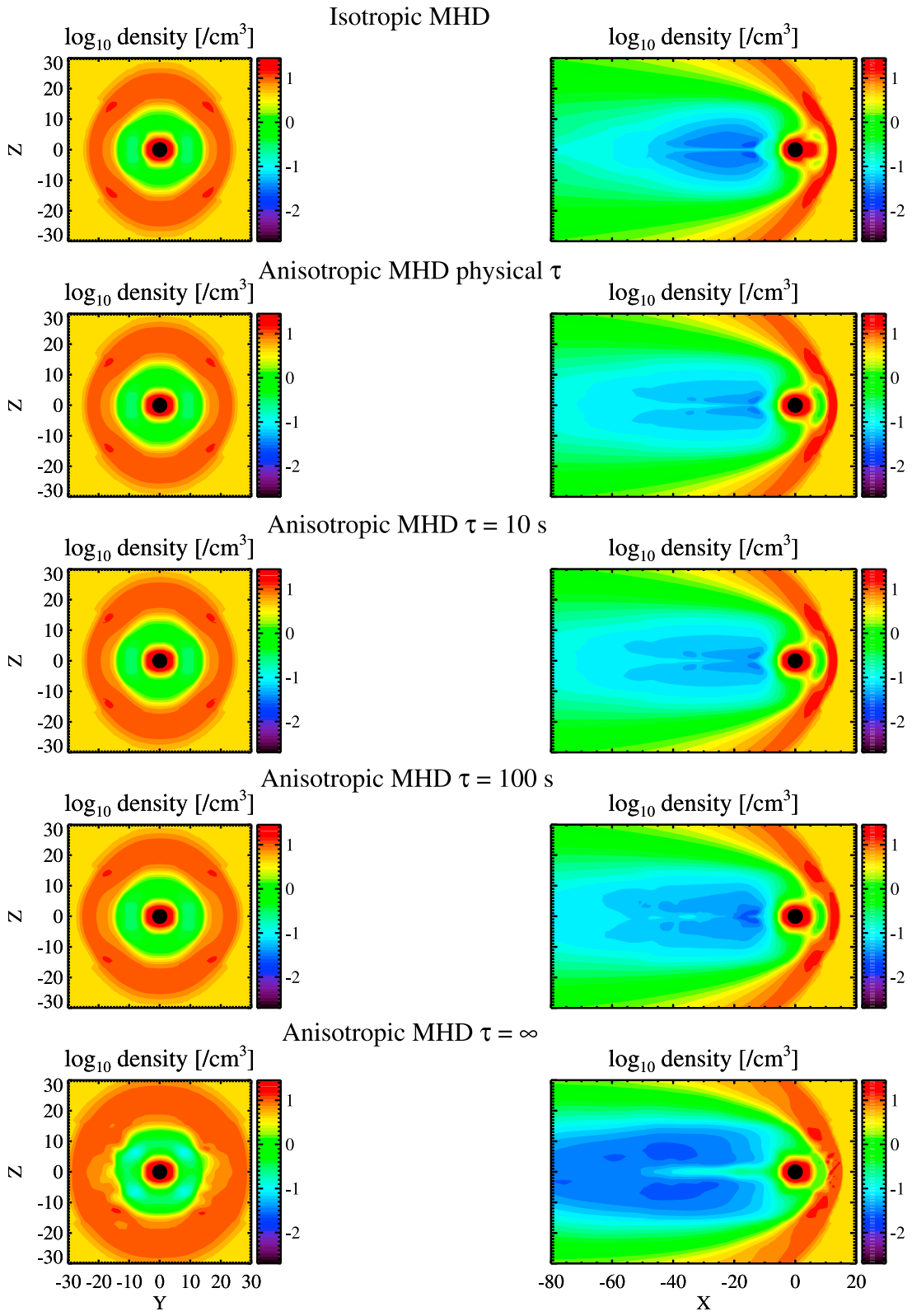

Figure 3. The logarithmic density contour in the $X = 0$ plane (left column) and the $Y = 0$ plane (right column) from the idealized magnetospheric simulations in the southward IMF case. Top to bottom: isotropic MHD, anisotropic MHD with physical τ based on the growth rates, anisotropic MHD with $\tau = 10$ s, anisotropic MHD with $\tau = 100$ s and anisotropic MHD with $\tau = \infty$.

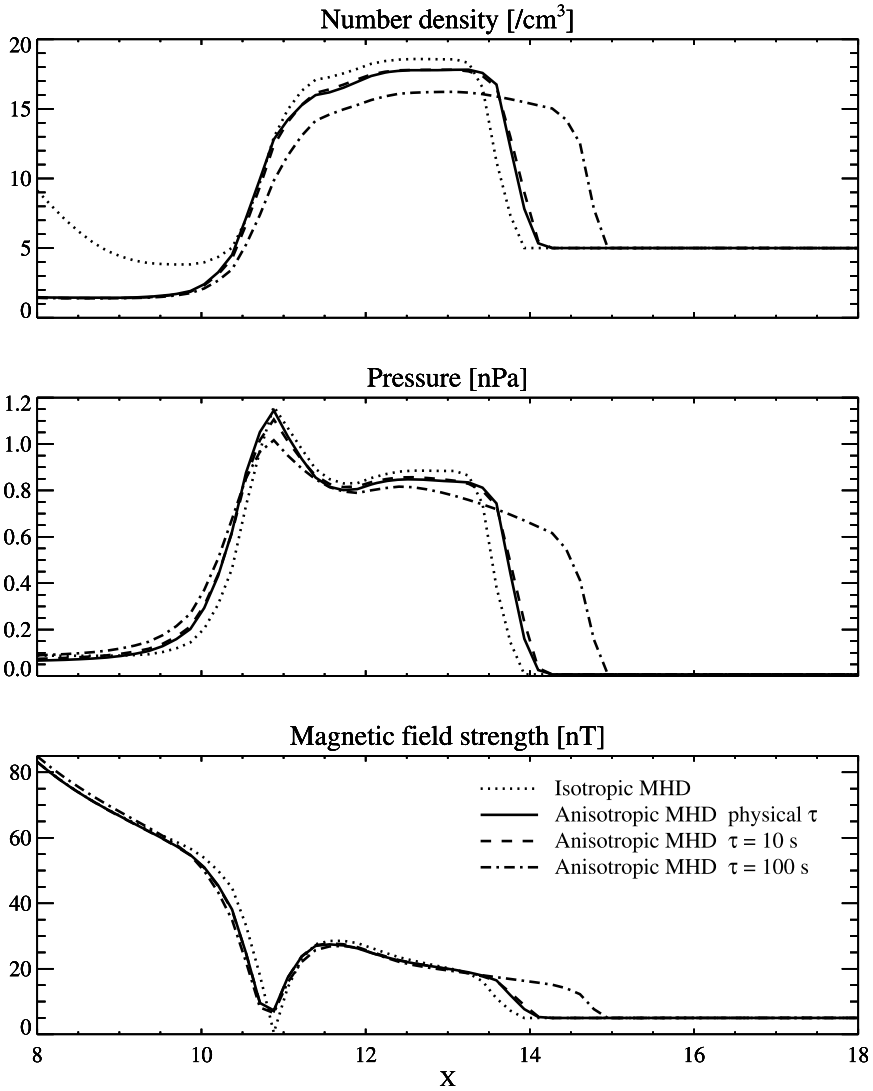

Figure 4. The number density (top), pressure (middle) and magnetic field strength (bottom) profiles of the dayside magnetosheath along the X axis from the idealized magnetospheric simulations in the southward IMF case. Different lines represent different runs as indicated in the figure.

derived the plasma pressure tensors from the Tsyganenko magnetic field models. *Lui et al.* [1994] obtained the perpendicular and parallel pressure distribution in force equilibrium with magnetic stresses from the Tsyganenko field models for the quiet time nightside magnetosphere. They found the deduced pressure profiles are in good agreement with the observations. The efforts of including pressure anisotropy in empirical modeling are successful and worthwhile, providing valid references and comparisons to our MHD modeling with anisotropic pressure.

[8] The following content of this paper is divided into three parts. For the sake of completeness, we begin by introducing the equation set for MHD with anisotropic pressure and its implementation into BATS-R-US in section 2. Then, in section 3, we present a variety of magnetospheric simulations performed using the anisotropic BATS-R-US model. These simulations cover the cases with idealized and real solar wind and IMF conditions as inputs. Finally, in section 4, we evaluate the model, propose future work and explore potential applications.

2. Methods

2.1. Background

[9] BATS-R-US is a global MHD model that can solve the idealized MHD equation set and its various extensions, for instance Hall, semirelativistic, multifluid and so on. It is also a part of the Space Weather Modeling Framework (SWMF) [*Tóth et al.*, 2012], a toolkit for the Sun-Earth environment modeling developed at the University of Michigan. For the Earth's magnetospheric simulations, BATS-R-US can be coupled with other physical components in the SWMF, including those modeling the ring current, the radiation belt, the ionospheric electrodynamics and the polar wind.

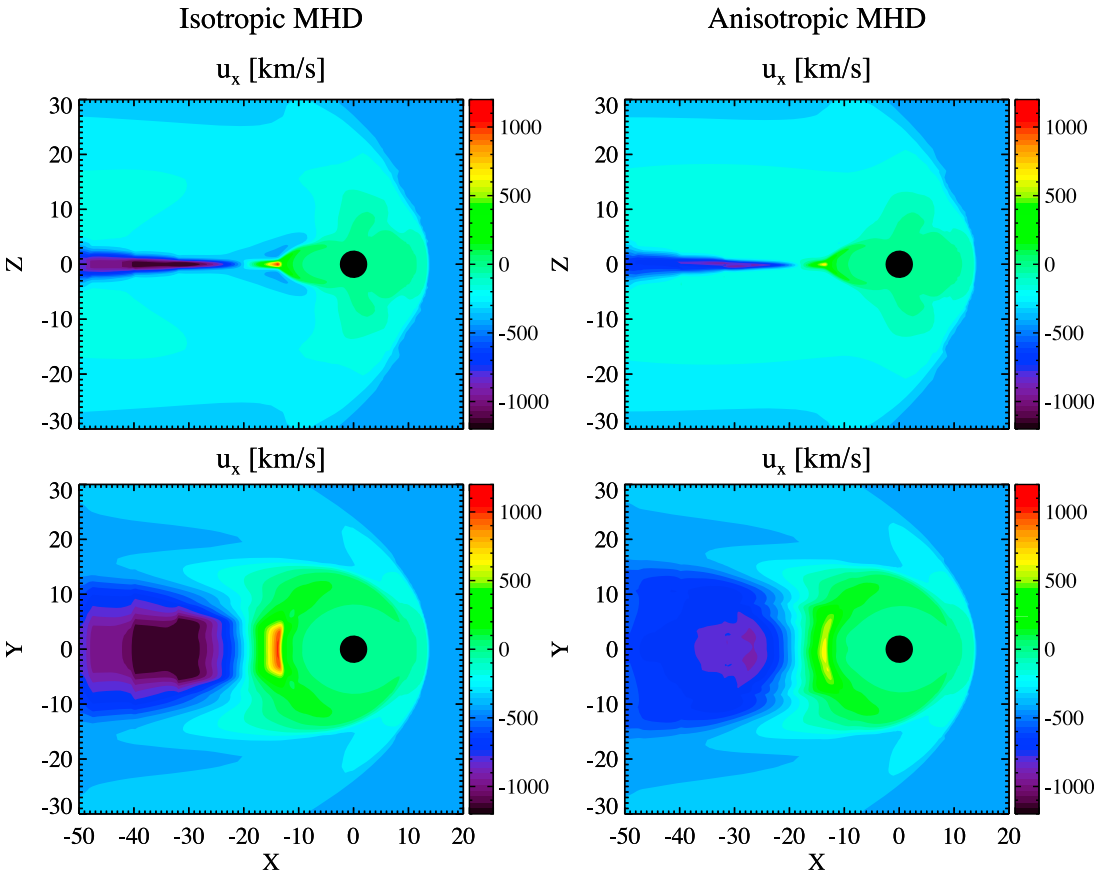

Figure 5. The x-direction velocity contour in the $Y = 0$ plane (top row) and the $Z = 0$ plane (bottom row) from the idealized magnetospheric simulations with isotropic MHD (left column) and anisotropic MHD with growth-rate based τ (right column) in the southward IMF case.

2.2. Equations

[10] As a newly implemented capability, BATS-R-US with anisotropic pressure solves the anisotropic MHD equations, which can be written as:

$$\frac{\partial \rho}{\partial t} + \nabla\cdot(\rho\mathbf{u}) = 0 \tag{1}$$

$$\frac{\partial \rho\mathbf{u}}{\partial t} + \nabla\cdot\left[\rho\mathbf{u}\mathbf{u} + p_\perp\mathbf{I} + (p_\parallel - p_\perp)\mathbf{b}\mathbf{b} - \frac{1}{\mu_0}\left(\mathbf{B}\mathbf{B} - \frac{B^2}{2}\mathbf{I}\right)\right] = 0 \tag{2}$$

$$\frac{\partial \mathbf{B}}{\partial t} + \nabla\times[-(\mathbf{u}\times\mathbf{B})] = 0 \tag{3}$$

$$\frac{\partial p_\parallel}{\partial t} + \nabla\cdot(p_\parallel\mathbf{u}) + 2p_\parallel\mathbf{b}\cdot(\mathbf{b}\cdot\nabla)\mathbf{u} = \frac{\delta p_\parallel}{\delta t} \tag{4}$$

$$\frac{\partial p}{\partial t} + \nabla\cdot(p\mathbf{u}) + \frac{2}{3}p_\perp(\nabla\cdot\mathbf{u}) + \frac{2}{3}(p_\parallel - p_\perp)\mathbf{b}\cdot(\mathbf{b}\cdot\nabla)\mathbf{u} = 0, \tag{5}$$

where ρ, $\mathbf{u}$ and $\mathbf{B}$ are the density, velocity and magnetic field, respectively. $\mathbf{b} = \mathbf{B}/|\mathbf{B}|$ is defined as the unit vector along the magnetic field. $p_\parallel$ represents the parallel pressure component with respect to the magnetic field, while p is the average scalar pressure. μ_0 denotes the permeability of vacuum. We take the polytropic index to be 5/3.

[11] We adopt the total scalar pressure p as one of the primitive variables for the sake of simplicity of the implementation and consistency with the ideal MHD case. The conversion between the total scalar pressure and the pressure components can be expressed as:

$$p = \frac{2p_\perp + p_\parallel}{3}. \tag{6}$$

Mathematically, we can use either $p_\parallel$ or $p_\perp$ as the other pressure variable as they make no difference. However, given $p_\perp$ is larger than $p_\parallel$ in most places where pressure anisotropy exists in the magnetosphere, the chance of $p_\parallel$ becoming negative when solving for p and $p_\perp$ is larger than the chance of $p_\perp$ getting negative when solving for p and $p_\parallel$. In favor of numerical computation, we choose to solve $p_\parallel$ instead of $p_\perp$.

[12] Compared to the ideal MHD equations, the momentum equation (2) and the total scalar pressure equation (5) are changed. Each of these equations contains a new term resulting from the difference between $p_\parallel$ and $p_\perp$: $(p_\parallel - p_\perp)\mathbf{b}\mathbf{b}$ in equation (2) and $\frac{2}{3}(p_\parallel - p_\perp)\mathbf{b}\cdot(\mathbf{b}\cdot\nabla)\mathbf{u}$ in equation (5). These two new terms are eliminated in the case of pressure isotropy, thus the equations reduce to the standard ideal MHD

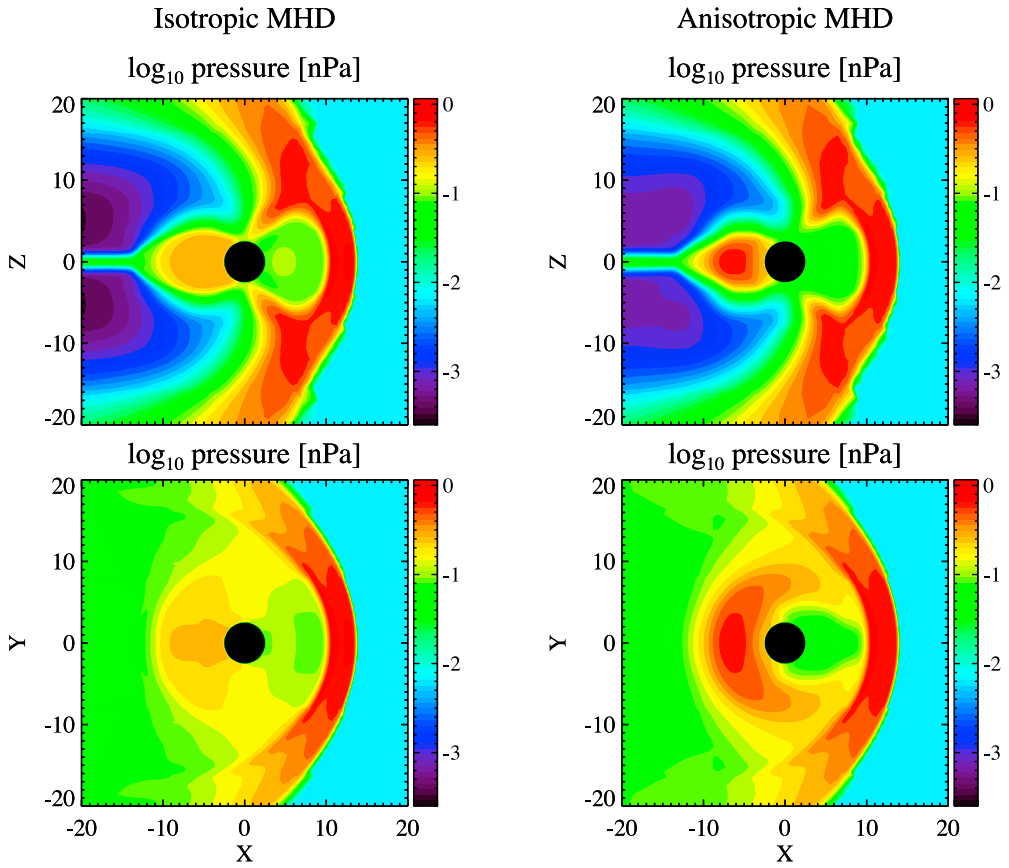

Figure 6. The logarithmic pressure contour in the $Y = 0$ plane (top) and the $Z = 0$ plane (bottom) from the idealized magnetospheric simulations with isotropic MHD (left column) and anisotropic MHD with growth-rate based τ (right column) in the southward IMF case.

equations as $p_\perp = p$. The right-hand side of equation (4) is the pressure relaxation term that will be discussed shortly. In the absence of the pressure relaxation term, equations (4) and (5) are equivalent to the double adiabatic equations.

[13] Capturing jump conditions across a discontinuity relies on acquiring conservation laws of the system. Therefore, we need to solve the conservative form of the equation set for the bow shock region. Only the pressure equations (4) and (5) are not in a conservation form. The conservation of energy density e provides the conservative equation that replaces total scalar pressure of equation (5) as:

$$\frac{\partial e}{\partial t} + \nabla\cdot\left[\mathbf{u}\left(e + p_\perp + \frac{\mathbf{B}^2}{2\mu_0}\right) + \mathbf{u}\cdot\left((p_\parallel - p_\perp)\mathbf{bb} - \frac{\mathbf{BB}}{2\mu_0}\right)\right] = 0 \tag{7}$$

with

$$e = \frac{\rho u^2}{2} + \frac{\mathbf{B}^2}{2\mu_0} + \frac{3}{2}p. \tag{8}$$

Compared to isotropic MHD, the total energy density equation also contains the additional term introduced by the pressure difference of the parallel and perpendicular components.

[14] However, the system is underdetermined as the parallel pressure equation (4) cannot be written in an appropriate conservative form. This particular issue has been discussed by many researchers [*Hudson*, 1970; *Chao and Goldstein*, 1972; *Lyu and Kan*, 1986; *Erkaev et al.*, 2000; *Vogl et al.*, 2001a, 2001b]. We solve equation (4), while using the instability criteria to bound the parallel pressure jump across the bow shock, similar to the bounded anisotropic fluid model proposed by *Denton et al.* [1994].

[15] Apart from supplementing the jump conditions, the plasma instabilities associated with anisotropic pressure limit the pressure anisotropy throughout the magnetosphere. We consider the firehose, the mirror, and the ion cyclotron instabilities, all of which can arise in plasmas with anisotropic pressure. The firehose instability occurs when [*Gary et al.*, 1998; *Lazar and Poedts*, 2009a, 2009b]

$$\frac{p_\parallel}{p_\perp} > 1 + \frac{\mathbf{B}^2}{\mu_0 p_\perp}. \tag{9}$$

The mirror and ion cyclotron instability criteria are [*Tajiri*, 1967; *Gary et al.*, 1976; *Gary*, 1992]

$$\frac{p_\perp}{p_\parallel} > 1 + \frac{\mathbf{B}^2}{2\mu_0 p_\perp} \tag{10}$$

and

$$\frac{p_\perp}{p_\parallel} > 1 + C_1\left(\frac{\mathbf{B}^2}{2\mu_0 p_\parallel}\right)^{C_2}, \tag{11}$$

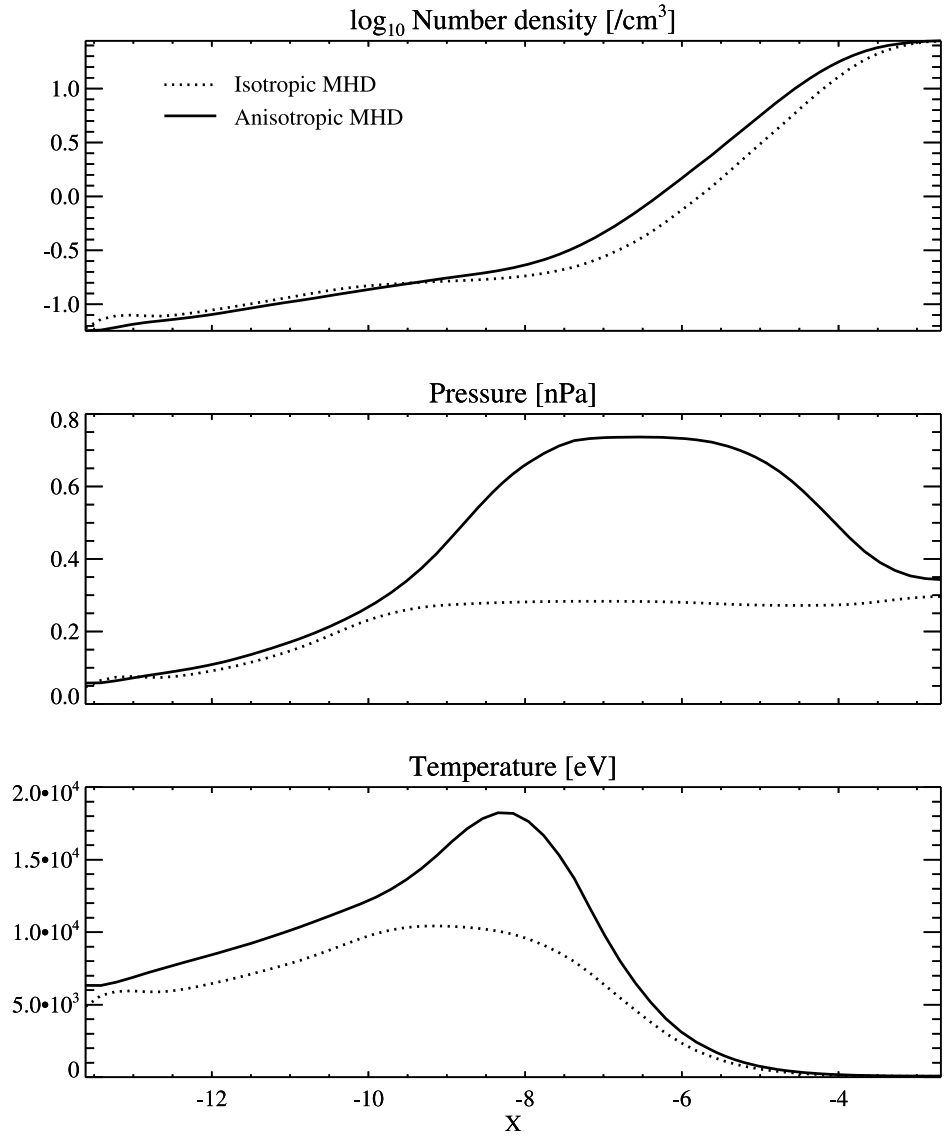

Figure 7. The number density (top), pressure (middle) and temperature (bottom) profiles of the nightside magnetosphere along the X axis from the idealized magnetospheric simulations with isotropic MHD (dotted line) and anisotropic MHD with growth-rate based τ (solid line) in the southward IMF case. For the anisotropic MHD case, we plot the scalar pressure as defined by equation (6) and the corresponding scalar temperature.

respectively, where we use $C_1 = 0.3$ and $C_2 = 0.5$ as they are close to the average values derived from observations in the magnetosphere [*Anderson et al.*, 1996; *Gary et al.*, 1995].

[16] The latter two instabilities involve kinetic effects and thus cannot be fully described by MHD. Moreover, the grid resolution that we normally apply in global MHD simulations may not be fine enough to resolve even hydromagnetic instabilities. The effect of these instabilities is represented by the collision term of the parallel pressure equation (4):

$$\frac{\delta p_{\parallel}}{\delta t} = \frac{\bar{p}_{\parallel} - p_{\parallel}}{\tau}, \tag{12}$$

where $\bar{p}_{\parallel}$ is the marginally stable parallel pressure obtained from equations (9), (10) or (11). We call equation (12) the pressure relaxation term due to the instabilities, with the relaxation time τ relates to their growth rates. In regions stable for all types of instabilities, the relaxation term (12) is zero. In unstable regions, the pressure relaxation term pushes the parallel pressure so that the plasma reaches the marginally stable states over time τ. In the case when both the mirror and ion cyclotron instabilities are present, only the one that gives larger $\delta p_{\parallel}/\delta t$ is applied. The details of how we set τ will be addressed in section 2.3.

[17] In addition to the pressure relaxation term applied in the unstable regions, we introduce a global pressure

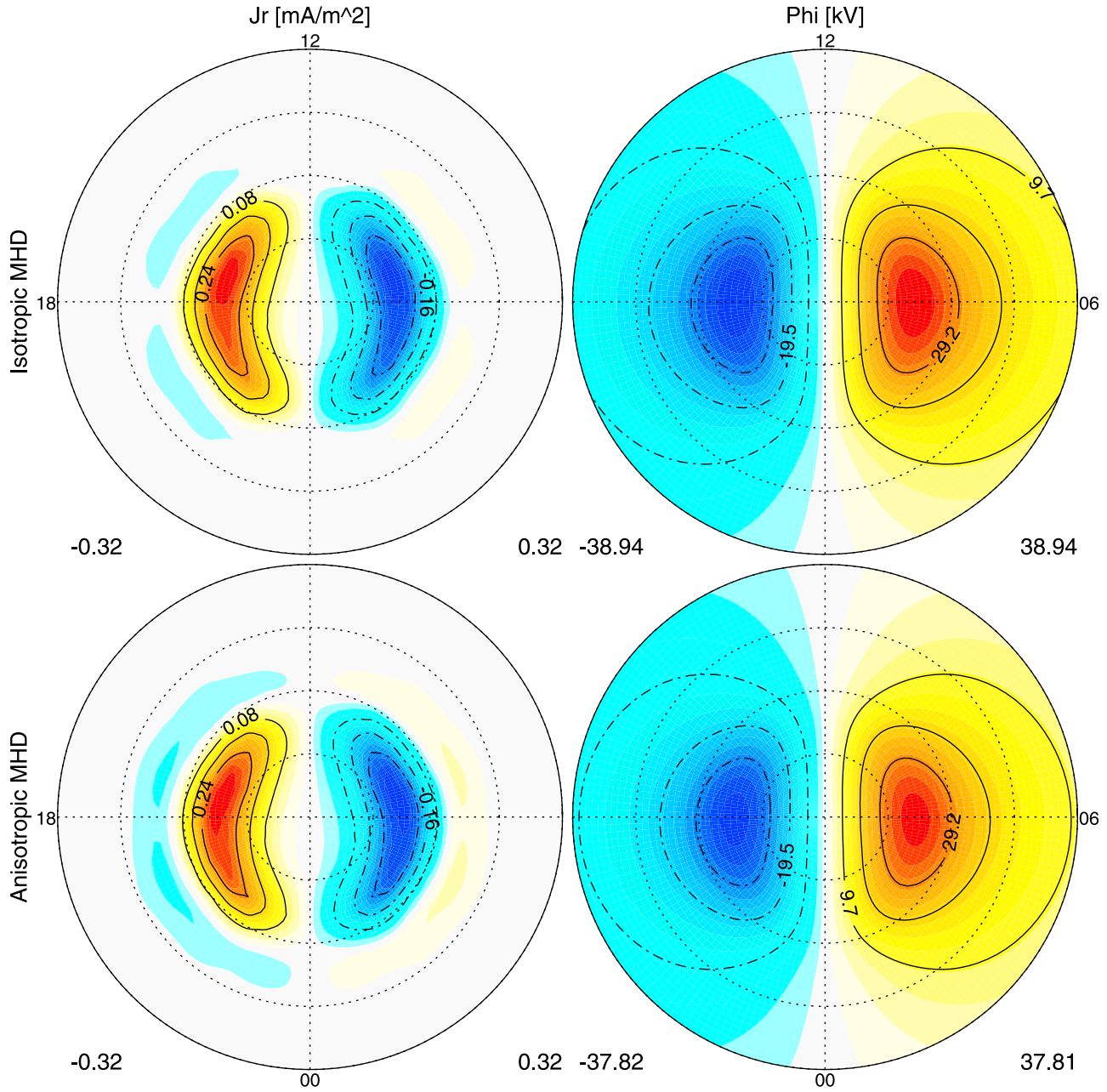

Figure 8. The ionospheric field-aligned currents (left column) and cross polar cap potential (right column) of the Northern Hemisphere from the idealized magnetospheric simulations with isotropic MHD (top) and anisotropic MHD with growth-rate based τ (bottom) in the southward IMF case.

relaxation term that applies everywhere to represent other possible mechanisms constraining the plasma pressure anisotropy in the real magnetosphere. We write the global relaxation term as

$$\frac{\delta p_{\parallel}}{\delta t} = \frac{p - p_{\parallel}}{\tau_g}, \tag{13}$$

where τ_g is the global relaxation time. In unstable regions, both (12) and (13) are computed, and the one with larger absolute value, which changes $p_{\parallel}$ more, is applied. To minimize the effect of the global relaxation term on the unstable regions, we set τ_g to be of the order of 100 s in quiet time magnetospheric simulations. According to the idealized simulations we performed, shown in section 3.1, the typical relaxation time τ due to the instabilities is much lower than 100 s.

[18] For the implementation into BATS-R-US, equations (1)–(5) and (7) are discretized with several numerical schemes. To deal with the case when the Alfvén speed is comparable or larger than the speed of light, including the

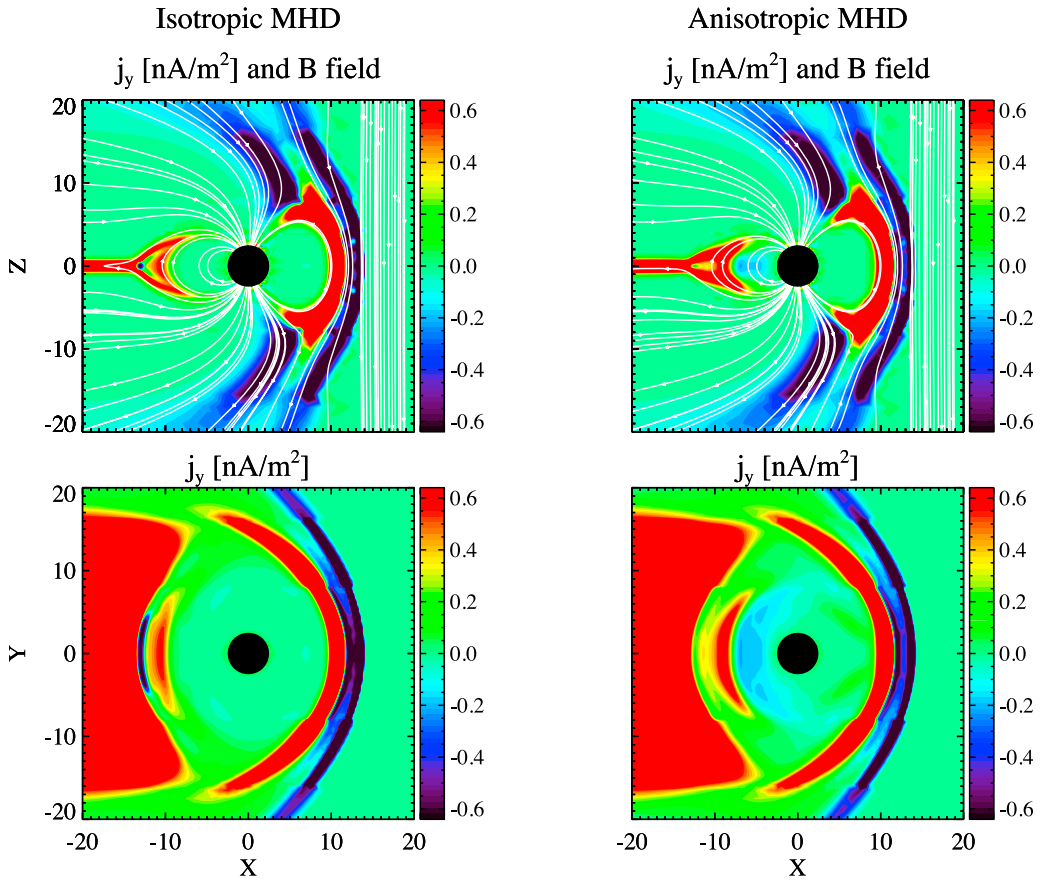

Figure 9. The Y-direction current density contour in the $Y = 0$ plane (top row) and the $Z = 0$ plane (bottom row) from the idealized magnetospheric simulations with isotropic MHD (left column) and anisotropic MHD with growth-rate based τ (right column) in the southward IMF case. The field lines are shown in the $Y = 0$ plane.

artificially reduced speed of light for the "Boris Correction" [*Boris*, 1970], we also implemented the semirelativistic formulation of MHD with anisotropic pressure. More details of the algorithm and implementation, as well as the series of numerical tests performed to verify the code can be found in *Meng et al.* [2012].

2.3. Anisotropy Relaxation Time

[19] We have implemented two types of relaxation time τ for the instability induced relaxation term (12). First, τ can be set to a constant value homogeneously in the computational domain. For magnetospheric simulations, typical values are of the order of 10 s, as we shall see later. Second, τ can be set based on the growth rates of the instabilities.

[20] For the firehose instability, the growth rate can be calculated from the dispersion relation of the Alfvén wave in a plasma with anisotropic pressure, written as [*Baranov*, 1970]:

$$\frac{\omega^2}{k_\parallel^2} = \frac{1}{\rho}\left(\frac{B^2}{\mu_0} + p_\perp - p_\parallel\right). \tag{14}$$

[21] When the firehose instability is excited—i.e., when equation (9) is satisfied—the growth rate is given by

$$\gamma_f = k_\parallel \sqrt{\frac{\Delta p_f}{\rho}}, \tag{15}$$

where $k_\parallel = k\cos\theta = (2\pi/\lambda)\cos\theta$, with θ representing the angle between the wave number $\mathbf{k}$ and the magnetic field, and $\Delta p_f = p_\parallel - p_\perp - B^2/\mu_0$.

[22] As the growth rate γ_f varies with the wavelength λ, we are seeking the wavelength that grows fastest. However, according to equation (15), the growth rate becomes infinity when the wavelength approaches zero. This is because the growth rate (equation (15)) is derived from the MHD theory that is valid only in the long-wavelength limit, i.e., the wavelength is much longer than the mean particle Larmor radius. Taking the finite Larmor radius effects into account, *Hall* [1979, 1981] showed that the growth rate is

$$\gamma_{f_{FLR}} = k_\parallel \sqrt{\frac{1}{\rho}\left\{\Delta p_f - \frac{1}{3\rho\Omega_i^2}\left[\frac{1}{4}p_\perp(p_\parallel - p_\perp)k_\perp^2 + p_\parallel\left(p_\perp - \frac{p_\parallel}{4}\right)k_\parallel^2\right]\right\}}, \tag{16}$$

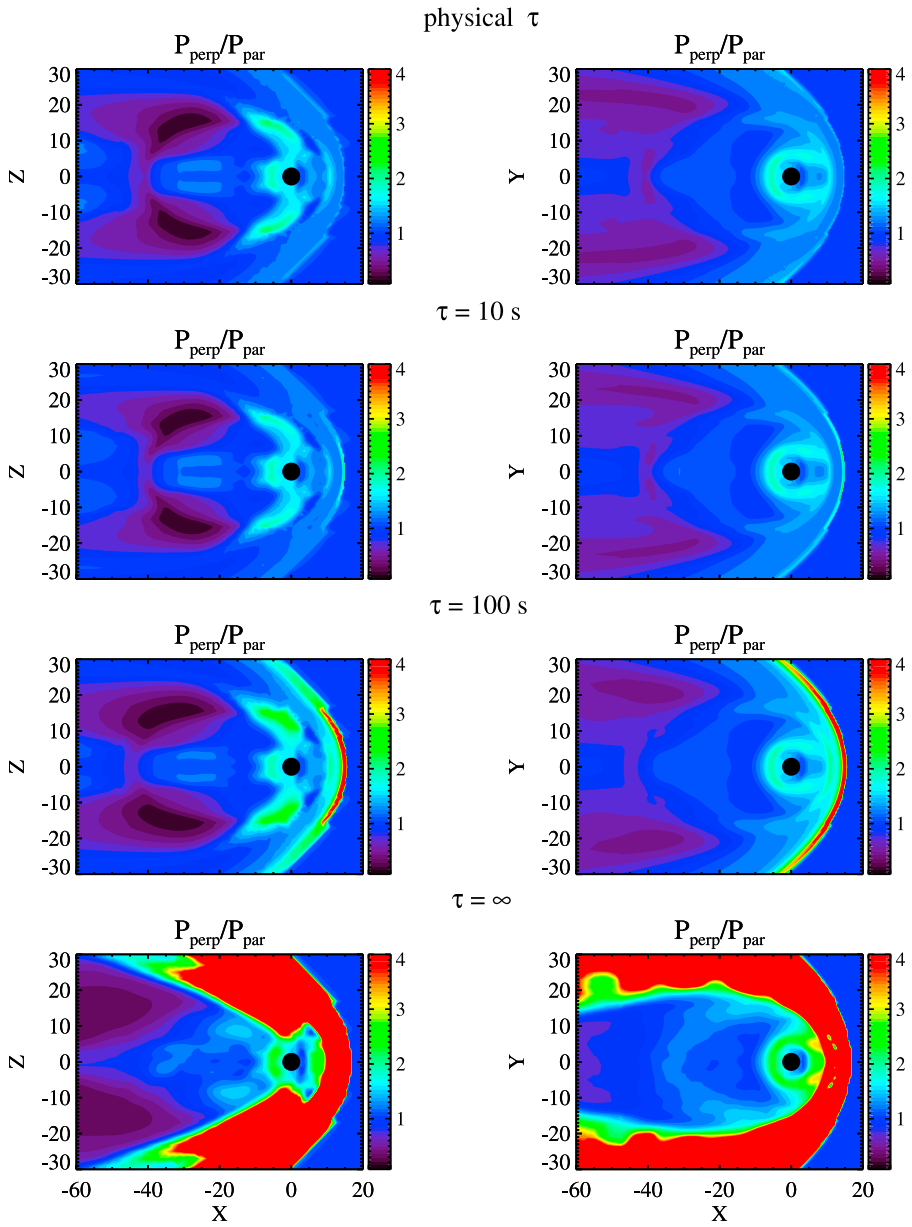

Figure 10. Same as Figure 1 for the northward IMF case.

where ρ is plasma density, $\Omega_i = qB/m$ is ion gyrofrequency, and $k_\perp = ksin\theta$. After some algebra, we found the maximum growth occurs when $\theta = 0$, for $p_\parallel / p_\perp < 4$, which shall hold true for the firehose instability in the magnetosphere. The corresponding fastest growing wavelength is obtained as

$$\lambda_f = 2\pi r_i \sqrt{\frac{6p_\parallel (p_\perp - p_\parallel/4)}{p_\perp \Delta p_f}}, \tag{17}$$

where $r_i = mv_\perp/(qB)$ is the ion Larmor radius.

[23] Based on the fastest growth rate, we write the relaxation time of the firehose instability as

$$\tau_f = \frac{1}{\gamma_{f_{FLR}}(\lambda_f)} = \frac{2}{\Omega_i} \frac{\sqrt{p_\parallel (p_\perp - p_\parallel/4)}}{\Delta p_f}. \tag{18}$$

In our single-fluid model, Ω_i is taken to be the gyrofrequency of a proton.

[24] A similar approach is applied to obtain the relaxation time for the mirror instability. The fluid description of this instability based on the MHD analysis yields the following growth rate [*Southwood and Kivelson*, 1993]

$$\gamma_m = k_\perp \sqrt{\frac{2p_\perp \Delta p_m}{p_\parallel \rho}}, \tag{19}$$

where $k_\perp = ksin\theta = (2\pi/\lambda)sin\theta$ and $\Delta p_m = (p_\perp - p_\parallel) - B^2 p_\parallel / (2\mu_0 p_\perp)$. Again the growth rate γ_m increases monotonically with k. Unfortunately, given the complicated expression for the growth rate with the finite Larmor radius effects [*Hall*, 1980], it is difficult to find the maximum growth rate.

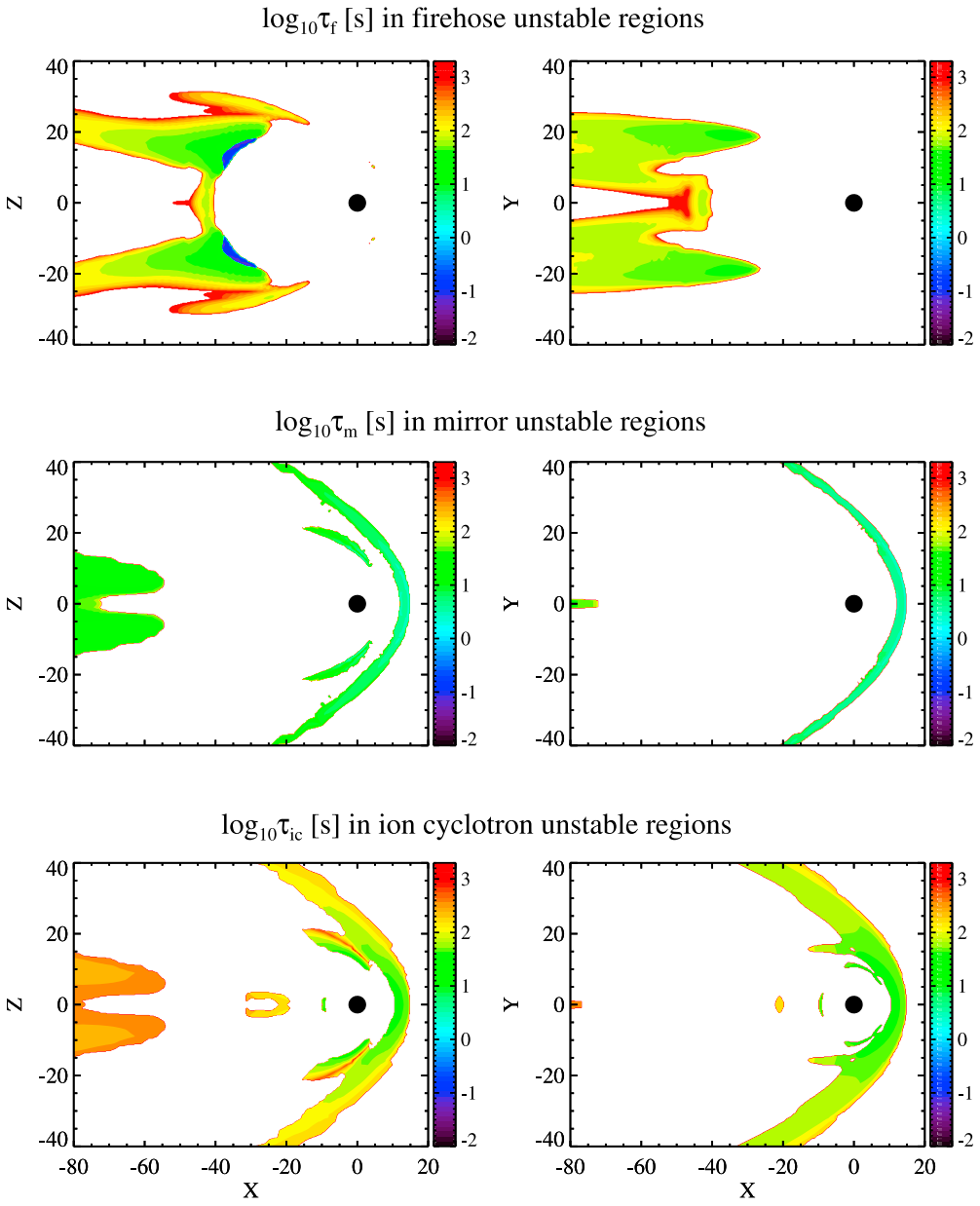

Figure 11. Same as Figure 2 for the northward IMF case.

However, Hall calculated the fastest growing wavelength assuming low pressure anisotropy and high plasma beta as

$$\lambda_m = \frac{3\sqrt{5}\pi}{2} r_i. \tag{20}$$

This is close to the typical values found from the full kinetic analysis by *Pokhotelov et al.* [2004], as shown in their Figure 1.

[25] Given λ_m is an order of magnitude larger than the ion gyroradius, we approximate the maximum growth rate from the long-wavelength MHD analysis by substituting (20) into (19). The relaxation time for the mirror instability is thus written as

$$\tau_m = \frac{1}{\gamma_m(\lambda_m)} = \frac{3\sqrt{5}}{4\Omega_i}\sqrt{\frac{p_\parallel}{2\Delta p_m}}. \tag{21}$$

[26] For the ion cyclotron instability, its growth rate varies with both the wavelength and the instability criterion (C_1 and C_2 in equation (11)) [*Gary et al.*, 1994]. In reality, the ion cyclotron instability can arise in the magnetosheath and the closed field line region near the Earth. However, the mirror instability often dominates over the ion cyclotron instability in the magnetosheath as observed and modeled [*Phan et al.*, 1994; *Shoji et al.*, 2009], which we have already taken care of. The only concern is for the inner magnetosphere. A good estimation of the relaxation time for the ion cyclotron instability should probably relate to the bouncing period of the particles travelling along the field lines. For sake of simplicity we approximate the growth rate based on observations in the magnetosphere [*Anderson*

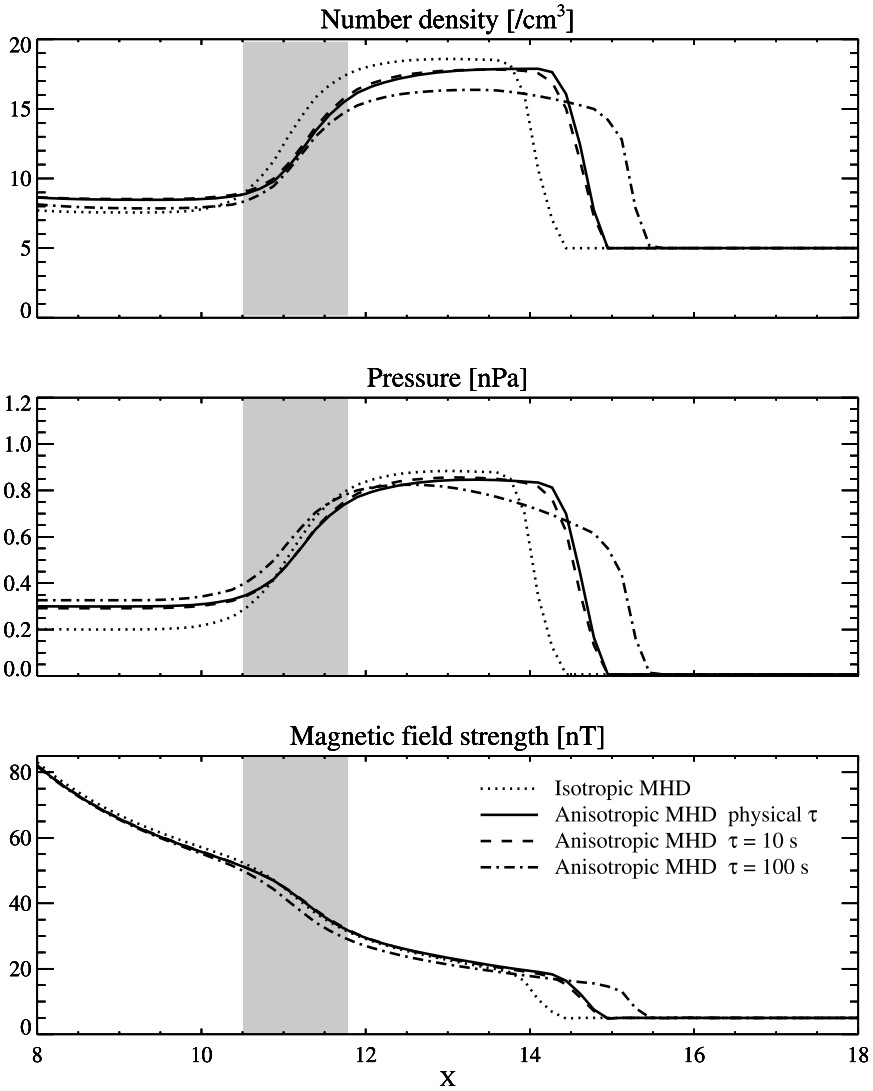

Figure 12. Same as Figure 4 for the northward IMF case.

et al., 1996] and theories [*Märk*, 1974; *Gary et al.*, 1993, 1995] as

$$\tau_{ic} = \frac{10^2}{\Omega_i}. \tag{22}$$

[27] Although the relaxation times (18), (21) and (22) have a physical basis, they are only approximations to the reality, so is the relaxation term (12). An underlying assumption is that the time rate of the change in the parallel pressure is the same as the growth rate of an instability. However, these simplifications are appropriate for our MHD model in terms of both computational cost and physical accuracy.

3. Global Magnetospheric Simulations

[28] To validate the anisotropic BATS-R-US code, we perform global magnetospheric simulations including idealized and real magnetosphere cases. All the simulations are produced from coupling BATS-R-US with the ionospheric electric potential solver Ridley Ionosphere Model (RIM) [*Ridley et al.*, 2004], i.e., the GM and IE components of the SWMF. Comparisons between the simulations and measurements are reported.

3.1. Idealized Magnetospheric Simulations

[29] Our model validation starts with simulating the magnetosphere under idealized conditions to exclude unnecessary factors that complicate the system. First, we neglect the rotation of the Earth. Second, we assume the magnetic axis aligns with the ecliptic North direction. Third, we use constant solar wind and interplanetary magnetic field (IMF) conditions through the simulations: number density ρ_{sw} = 5/cc, temperature $T_{sw} = 10^5$ K, velocity $u_{xsw} = -400$ km/s, $u_{ysw} = u_{zsw} = 0$ and purely southward IMF $B_{zsw} = -5$ nT or northward IMF $B_{zsw} = 5$ nT. The input solar wind pressure is assumed to be isotropic. Finally, for the ionosphere we apply constant Pedersen conductance 5 mho and neglect Hall conductance.

[30] The computational domain is a three-dimensional box in GSM coordinates. With the Earth at the origin, the box

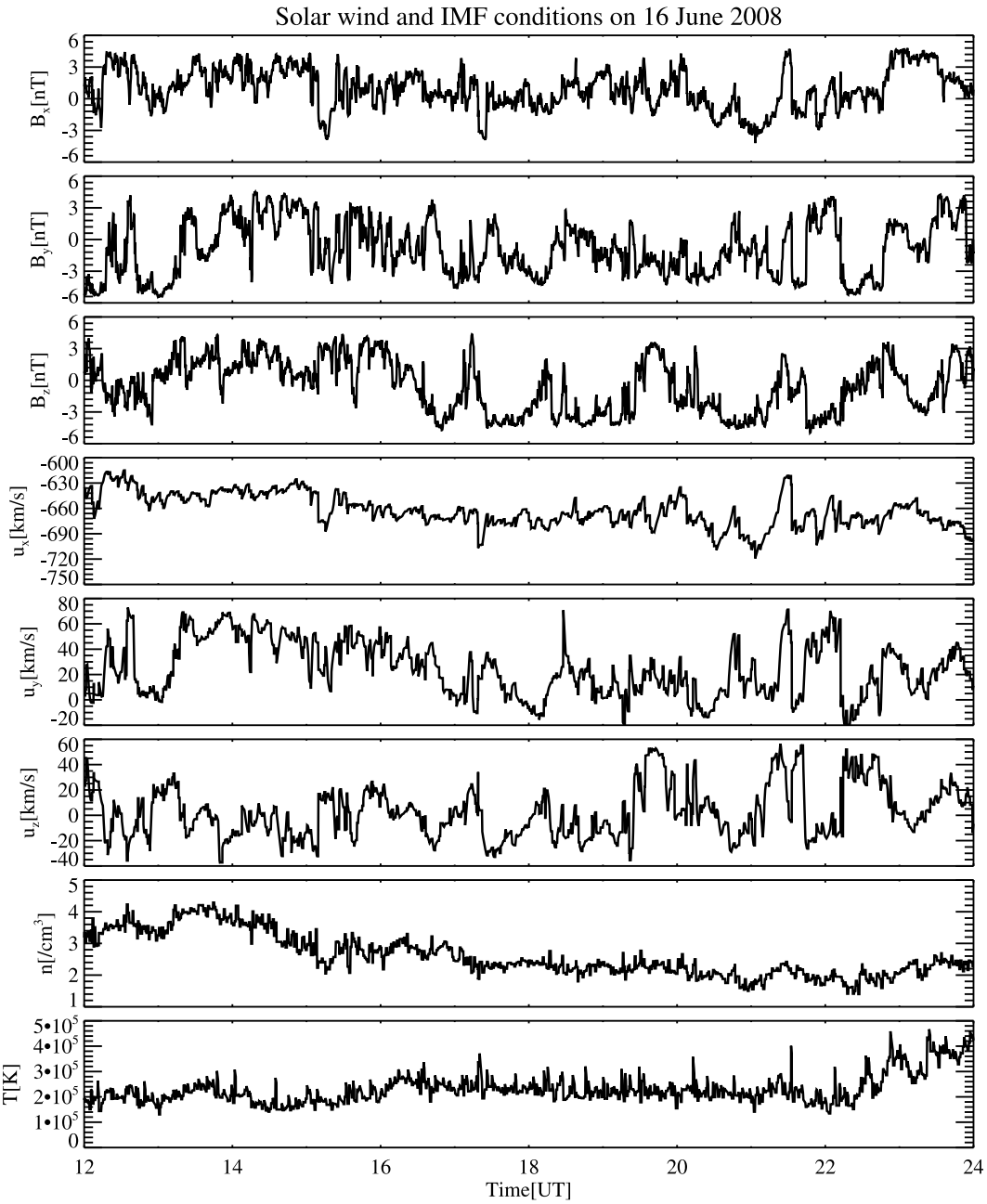

Figure 13. The solar wind and IMF conditions from ACE data for 12:00–24:00 UT on 16 June 2008.

covers from −224 to 32 Earth radii (R_e) in the X direction and from −64 to 64 R_e in the Y and Z directions. The inner boundary is the surface of a sphere surrounding the Earth at a radius of 2.5 R_e, where the density is set to be 28/cc. Taking advantage of the adaptive mesh refinement (AMR) in BATS-R-US, we set the finest resolution of 1/4 R_e near the Earth and the coarsest resolution of 4 R_e far down the tail. We take the Boris factor to be 0.01, i.e., the reduced speed of light is 3000 km/s. We use the Sokolov scheme [*Sokolov et al.*, 2002] with the Koren limiter [*Koren*, 1993] in all idealized runs. We do not apply the global pressure relaxation term (13), so the pressure anisotropy is only limited by the instabilities, if present, based on (12).

3.1.1. Southward IMF Case

[31] To investigate the effects of the pressure relaxation term (12) we compute four runs identically except with different relaxation times. One of them uses the growth-rate dependent relaxation times for the three instabilities as (18), (21) and (22); The other three use a constant relaxation time of τ = 10 s, 100 s, ∞ (no relaxation term at all) for all three instabilities. For comparisons, we also produce a run using standard BATS-R-US with isotropic pressure. All five runs starts with 5000 iterations in steady state mode before they are switched to time accurate mode lasting for 4 hours in physical time. We analyze the results at the end of the simulations.

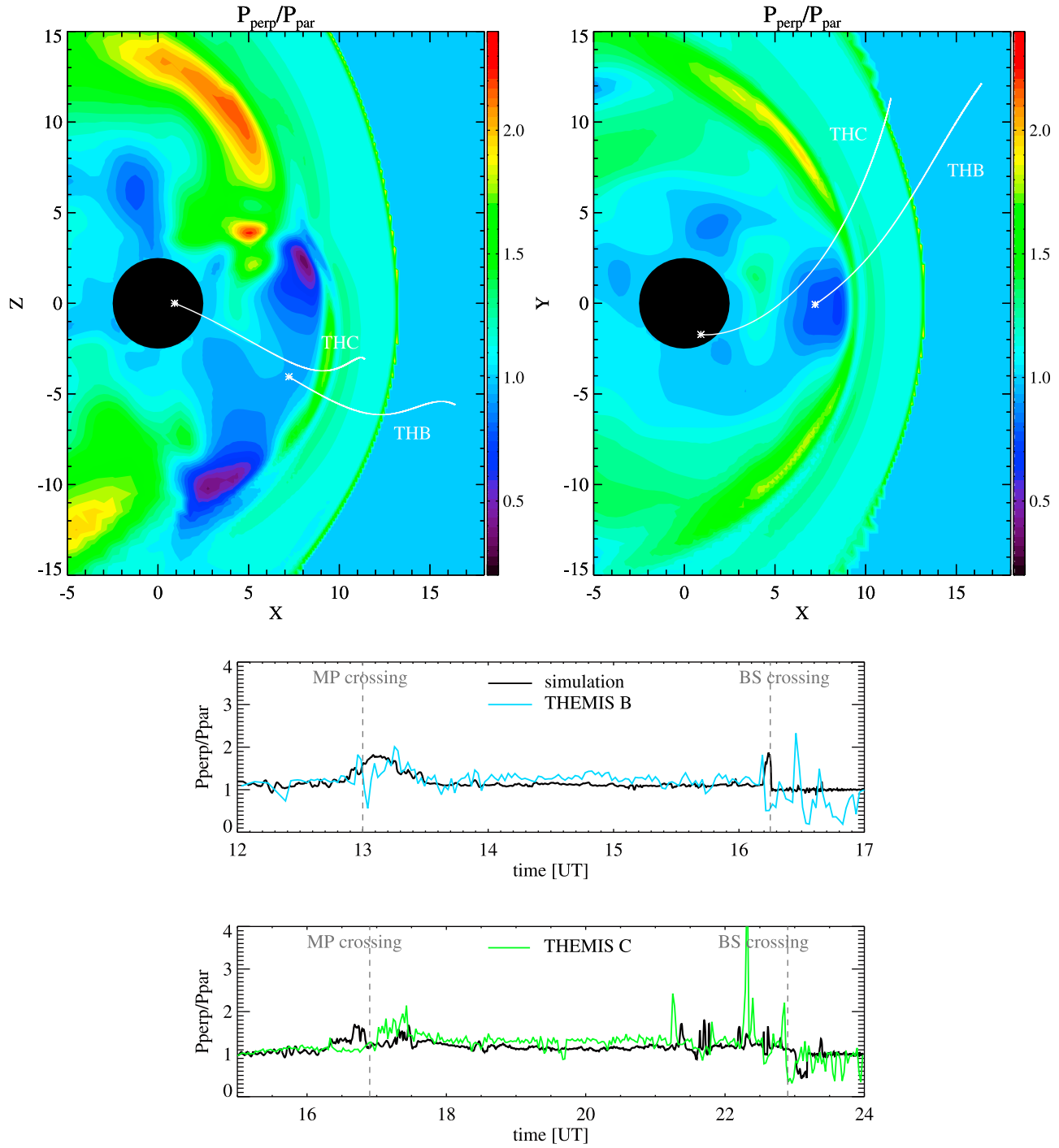

Figure 14. The pressure anisotropy ratio $p_\perp / p_\parallel$ in the $Y = 0$ (top left) and $Z = 0$ (top right) planes at 18:00 UT on 16 June 2008. Trajectories of THEMIS B and C during 12:00–24:00 UT are shown by white lines started from the stars. The two bottom panels show the simulated $p_\perp / p_\parallel$ (black lines) against the actual data along the satellite trajectories.

[32] First we examine the pressure anisotropy. Figure 1 shows the pressure anisotropy ratio $p_\perp / p_\parallel$. We extract the solutions in the noon-midnight meridional plane $Y = 0$ (left column) and the equatorial plane $Z = 0$ (right column) from the four runs with different relaxation times. To have a better visualization for all cases, the color scale is saturated for $p_\perp / p_\parallel > 4$. In the $\tau = 100$ s and $\tau = \infty$ cases, $p_\perp / p_\parallel$ reaches a maximum of 15 and 200 in the magnetosheath, respectively, which are highly unrealistic values. The $\tau = 10$ s case gives a little higher $p_\perp / p_\parallel$ compared to the growth-rate based τ case, thus an appropriate constant τ should be a few seconds. Essentially, three regions develop highly perpendicular pressure: the magnetosheath, the cusps and the magnetotail reconnection site. These regions are filled with compressed flow, thus the perpendicular pressure increases [*Hesse and Birn*, 1992].

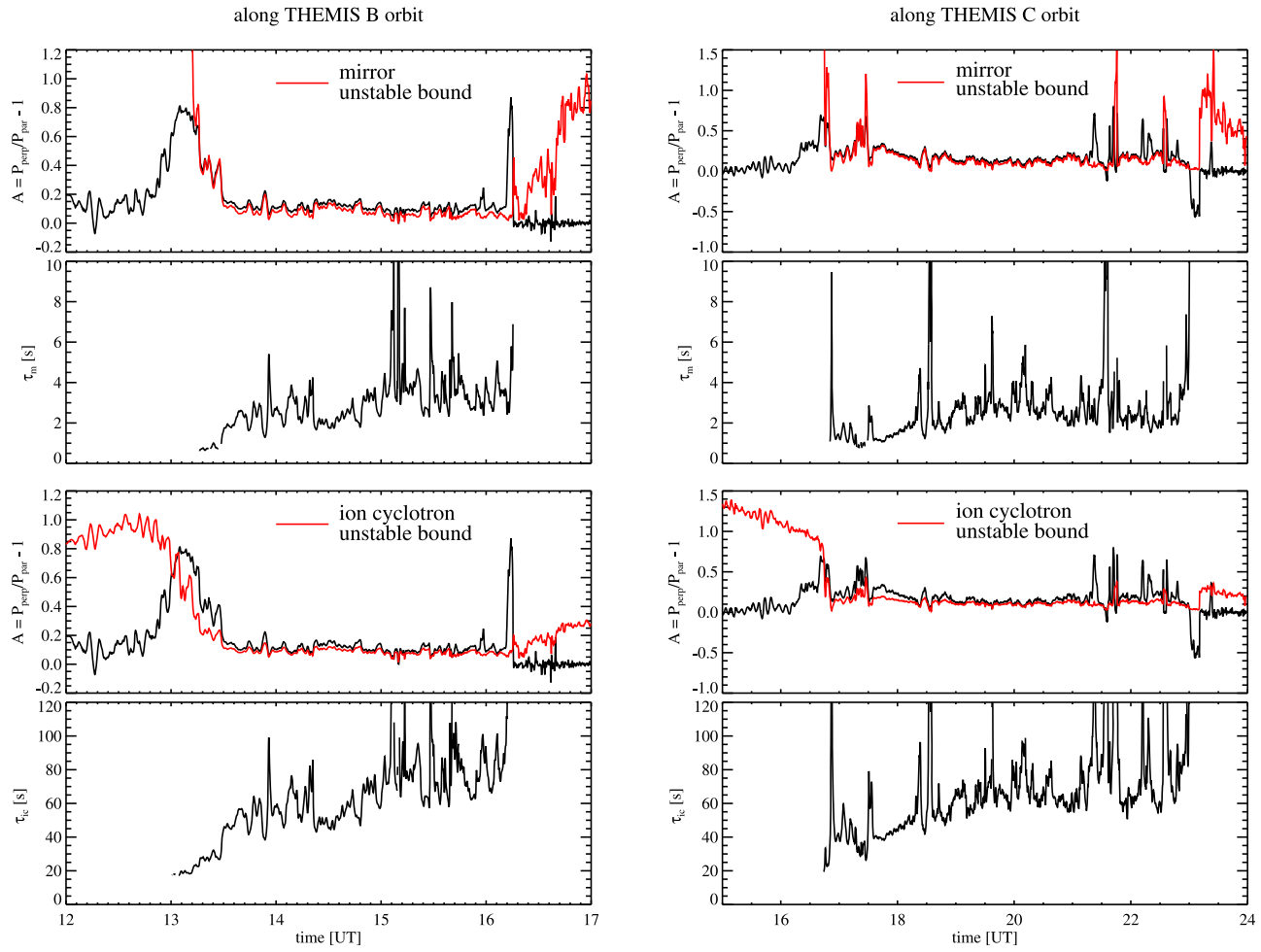

Figure 15. The simulated anisotropy factor A (black lines in the first and third rows from top), the unstable bounds (red lines) and the relaxation time (the second and fourth rows from top) along THEMIS B and C orbits during 12:00–24:00 UT on 16 June 2008.

[33] Next we look into the spatial variation of τ in the growth-rate based τ case, as displayed in Figure 2. We plot τ for three instabilities as color contours on the noon-midnight meridional plane and the equatorial plane. The white regions are stable with infinite τ. The relaxation term (12) is only applied in the unstable regions as colored with the corresponding τ value. The firehose instability (first row) only arises in very limited regions of the dayside magnetosphere and in the distant tail, with τ_f varying from about 10 s to hundreds of seconds. Both the mirror (middle row) and ion cyclotron instabilities exist throughout the magnetosheath and in the tail reconnection region. In the magnetosheath and the tail reconnection region, τ_m (around a few seconds) is much smaller than τ_{ic} (hundreds of seconds). Compared to the mirror instability region, the ion cyclotron instability region extends into the inner magnetosphere, but it does not include the region very close to the Earth. This is probably due to the strong magnetic field near the Earth that stabilizes the plasma, as can be seen in the stability condition (11).

[34] To have more insight into the differences between anisotropic and isotropic MHD in global models, we compare the results from these two types of simulations. For anisotropic MHD we refer to the run with growth-rate based relaxation time unless otherwise specified. The most prominent distinctions are:

[35] 1. The width and shape of the magnetosheath. Previous 2-D and 3-D anisotropic MHD simulations of the magnetosheath [*Erkaev et al.*, 1999; *Denton and Lyon*, 2000; *Samsonov and Pudovkin*, 2000] have observed a thicker magnetosheath than isotropic MHD simulations give. Our results agree with it. Moreover, with global simulations, we are able to examine the effects of pressure anisotropy on the shape of the whole magnetosphere.

[36] Figure 3 shows density contours in the $X = 0$ and $Y = 0$ planes. As the constant relaxation time τ increases, i.e., higher pressure anisotropy is allowed in the system, the magnetosheath, shown as the red region, becomes thicker. At the same time, the magnetosheath grows faster in the Y direction than in the Z direction, such that the boundary of the magnetosphere in the $X = 0$ cut changes from an oval to a circle. This is due to the larger pressure along the Y direction than the one along the Z direction, since the pressure perpendicular to the magnetic field, which is mostly along the Z direction, is larger than the pressure parallel to the magnetic field in the magnetosheath.

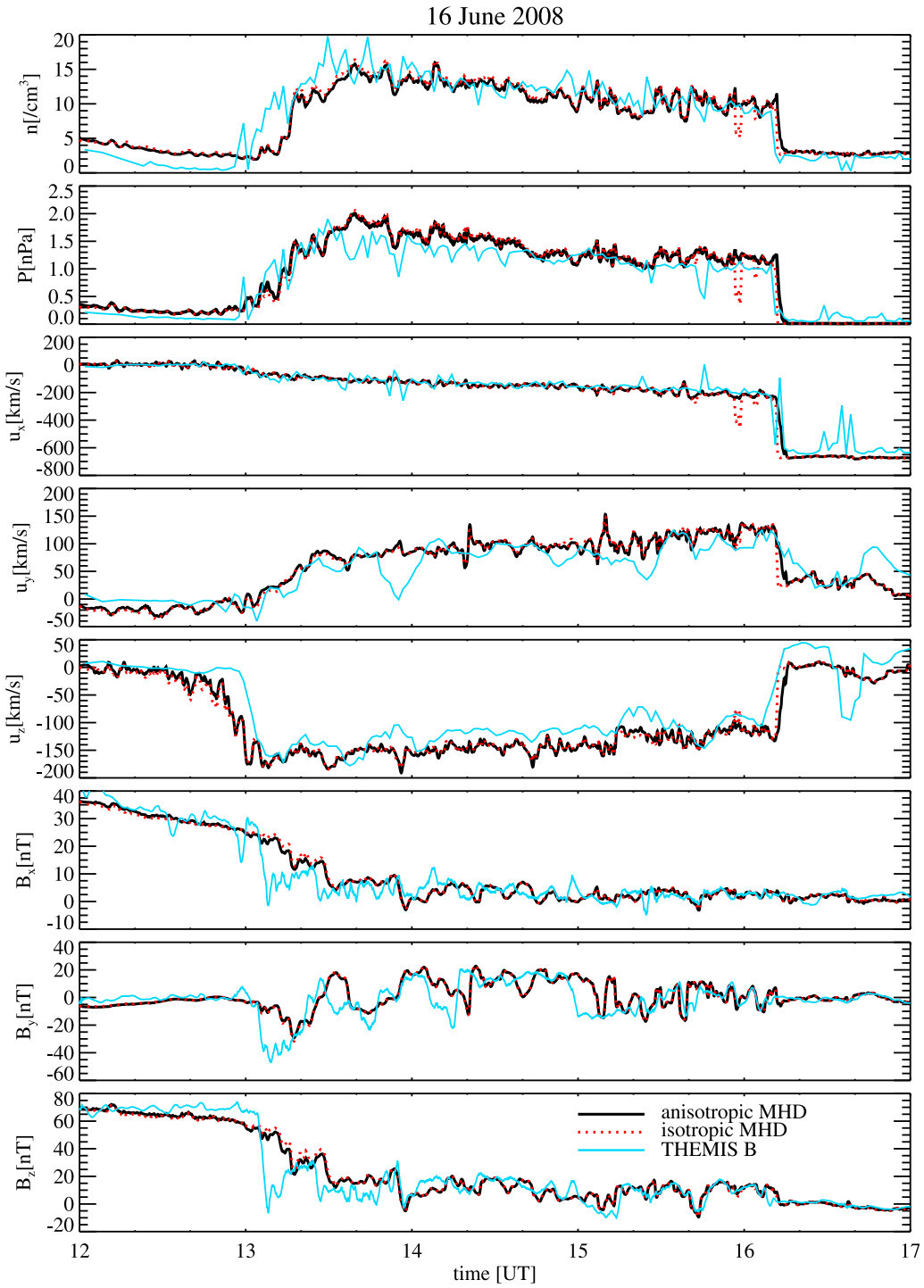

Figure 16. The simulated and measured variables along the THEMIS B orbit during 12:00–24:00 UT on 16 June 2008.

[37] The thickening of the magnetosheath can also be identified in Figure 4 that shows the variations of the variables along the X axis. The $\tau = \infty$ case is not shown as it is too far from the reality. The density and pressure profiles of different τ and their comparisons with isotropic MHD results clearly indicate the trend of the increasing width of the sub-solar magnetosheath. For the realistic τ = 10s setting, represented by the dashed line, the profiles are very close to the profiles of the growth-rate based τ case represented by the solid line. Both cases are reasonably close to the isotropic MHD solution shown by the dotted line except the region inside the magnetosphere, where isotropic MHD produces higher density. Compared to the isotropic case, the anisotropic MHD simulation with growth-rate based τ slightly widens the subsolar magnetosheath. Figure 4 also indicates that the anisotropic MHD model yields smaller density and pressure across the magnetosheath.

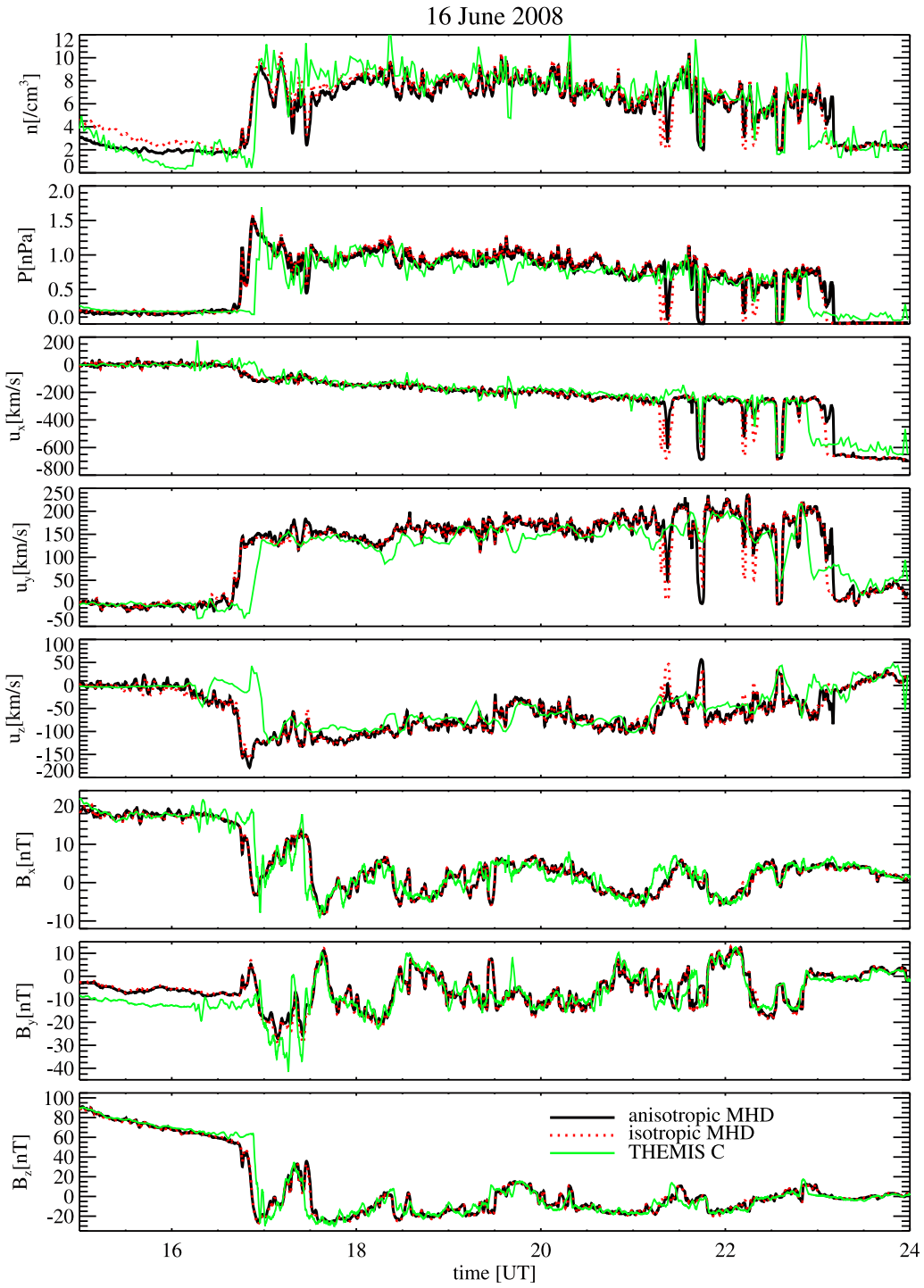

Figure 17. The simulated and measured variables along the THEMIS C orbit during 12:00–24:00 UT on 16 June 2008.

[38] 2. The speed of the earthward plasma jet from the tail. The standard isotropic MHD simulation generates high-speed plasma jets from the tail reconnection site toward the Earth and the far tail. The speed reaches a highly unrealistic value of 1000 km/s, as Figure 5 shows in the left column. Observations give the typical tail flow speed smaller than 300 km/s during quiet time [*Baumjohann and Pashmann*, 1989], as also shown in our February 2009 event later. Higher speeds are only observed intermittently [*Angelopoulos et al.*, 1994]. The anisotropic MHD simulation shown in the right column significantly reduces this speed to about half. As these plasma jets are produced directly by the tail magnetic reconnection, slower jets imply a weaker reconnection. A qualitatively similar behavior was observed by *Birn et al.* [2001], who have found that pressure anisotropy leads to reduced growth rate of magnetic islands

Table 1. RMS Errors of the Simulated Variables: 16 June 2008 Event

	THEMIS B		THEMIS C	
	Isotropic MHD	Anisotropic MHD	Isotropic MHD	Anisotropic MHD
n [/cc]	2.18	2.29	1.66	1.66
u_x [km/s]	63.37	52.93	80.21	74.22
u_y [km/s]	37.67	36.45	46.68	45.23
u_z [km/s]	45.48	46.12	42.52	42.30
b_x [nT]	5.81	5.52	3.95	3.93
b_y [nT]	11.75	11.77	6.85	6.70
b_z [nT]	11.57	10.86	10.13	10.32

in their study for the Geospace Environment Modeling (GEM) magnetic reconnection challenge.

[39] 3. The magnitude and distribution of the nightside plasma pressure. Figure 6 displays pressure contours in the $Y = 0$ and $Z = 0$ planes. First, the nightside plasma pressure of the anisotropic MHD simulation is stronger than that in the isotropic MHD simulation. This agrees with the empirical modeling result reported by *Lui et al.* [1994], who found the inclusion of pressure anisotropy in empirical magnetic field models increases the plasma pressure in the quiet time nightside magnetosphere. In our anisotropic MHD simulation, the nightside pressure is mostly contributed by the perpendicular pressure given $p_\perp / p_\parallel > 1$ in this region (see Figure 1). Unlike the anisotropic MHD case, in which the perpendicular pressure can evolve differently from the parallel pressure, the traditional isotropic MHD forces the pressure in the inner magnetosphere to be isotropic thus limits the magnitude of the pressure, which directly affects the field-aligned currents in the ionosphere as we shall see later.

[40] Second, compared to the pressure distribution from the isotropic MHD simulation, the anisotropic MHD simulation has a peak in total scalar pressure at around $-7\ R_e$. A clearer view is given by the middle panel of Figure 7, in which the nightside pressure profiles are extracted along the X axis from the two simulations denoted by the dotted and the solid lines, respectively. The anisotropic MHD simulation has almost three times larger pressure at $-7\ R_e$ than the isotropic MHD simulation does. The latter shows no peak in the pressure distribution. This difference leads to different pressure gradients, and furthermore different ring current patterns in the two simulations. Figure 7 also shows the density and temperature profiles along the X axis in the nightside. For the anisotropic MHD case, the total scalar temperature is plotted. The anisotropic MHD run produces hotter nightside plasma.

[41] 4. The magnitudes of the field-aligned currents and the cross polar cap potential. The anisotropic MHD simulation generates stronger region 2 currents compared to the isotropic simulation, as shown by the ionospheric view over the northern hemisphere in the left column of Figure 8. This is expected from the stronger nightside pressure in the anisotropic MHD simulation, since the nightside plasma contributes to the region 2 currents through the partial ring current. In addition, the cross polar cap potential shown in the right column of Figure 8 is slightly less in the anisotropic MHD case (the lower plot) than in the isotropic MHD case (the upper plot).

[42] 5. The pattern of the ring current. As mentioned before, the different pressure distributions from the anisotropic MHD and isotropic MHD simulations result in different ring current patterns in these two cases. In general, the anisotropic MHD case will give stronger ring current as the pressure gradient is larger than that of the isotropic case. A more strict analysis should consider the individual contributors to the ring current. For isotropic MHD, only the gradient of the pressure plays a role. For anisotropic MHD, both the gradient of the perpendicular pressure and another term involving the difference between the perpendicular and parallel pressures contribute to the ring current. The additional term in anisotropic MHD introduces an eastward ring current, which make the original westward ring current peak away from the equator, as found by Cheng and confirmed by Zaharia in their equilibrium model [*Cheng*, 1992; *Zaharia et al.*, 2004]. Our anisotropic MHD simulation produces the same phenomenon.

[43] In Figure 9, the Y-direction current density, as an indicator of the ring current density, is shown in the meridional and equatorial planes. The color scale is saturated for j_y above 0.64 nA/m^2 and below -0.64 nA/m^2. The westward current (in red) at around $-9\ R_e$ is much more prominent in the anisotropic MHD case. It peaks away from the equator and extends to higher latitude along the field lines. Meanwhile an eastward current (in blue) peaked at the equator at around $-7\ R_e$ appears in the anisotropic MHD case, which is contributed from both the perpendicular pressure gradient and the additional pressure anisotropy term. The magnitude of the eastward current (around 0.3 nA/m^2) is smaller than the observed values (about 1 nA/m^2) from *Lui and Hamilton* [1992]. The discrepancy is expected given the lack of an inner magnetospheric model.

3.1.2. Northward IMF Case

[44] For the northward IMF case, we also perform a set of five runs. All parameters remain the same as the southward IMF case except the change in the IMF orientation.

[45] The pressure anisotropy in the meridional and equatorial planes is shown in Figure 10. Again we observe highly perpendicular pressure in the magnetosheath and in the vicinity of the Earth. Increased relaxation time τ leads to increased pressure anisotropy. The $\tau = 10$ s run is most similar to the growth-rate based τ run. In the $\tau = 100$ s and $\tau = \infty$ simulations, the maximum of $p_\perp / p_\parallel$ is much larger than 4 such that the anisotropy ratio is saturated on the color scale.

[46] Figure 11 displays the spatial variation of τ. Most of it is very similar to the southward IMF case, except no mirror instability is excited in the close tail. The magnitude of τ varies between less than 1 second to hundreds of seconds, depending on the location.

[47] The effect of pressure anisotropy on the width of the magnetosheath is shown in Figure 12. Similar to the southward IMF case, the increased pressure anisotropy results in a thicker magnetosheath. However, compared to Figure 4, the width of the magnetosheath is more sensitive to pressure anisotropy in the northward IMF case, as the same amount of relaxation time τ results in a larger change of the magnetosheath position in the northward IMF case than in the southward IMF case. An exception occurs when $\tau = 100$ s,

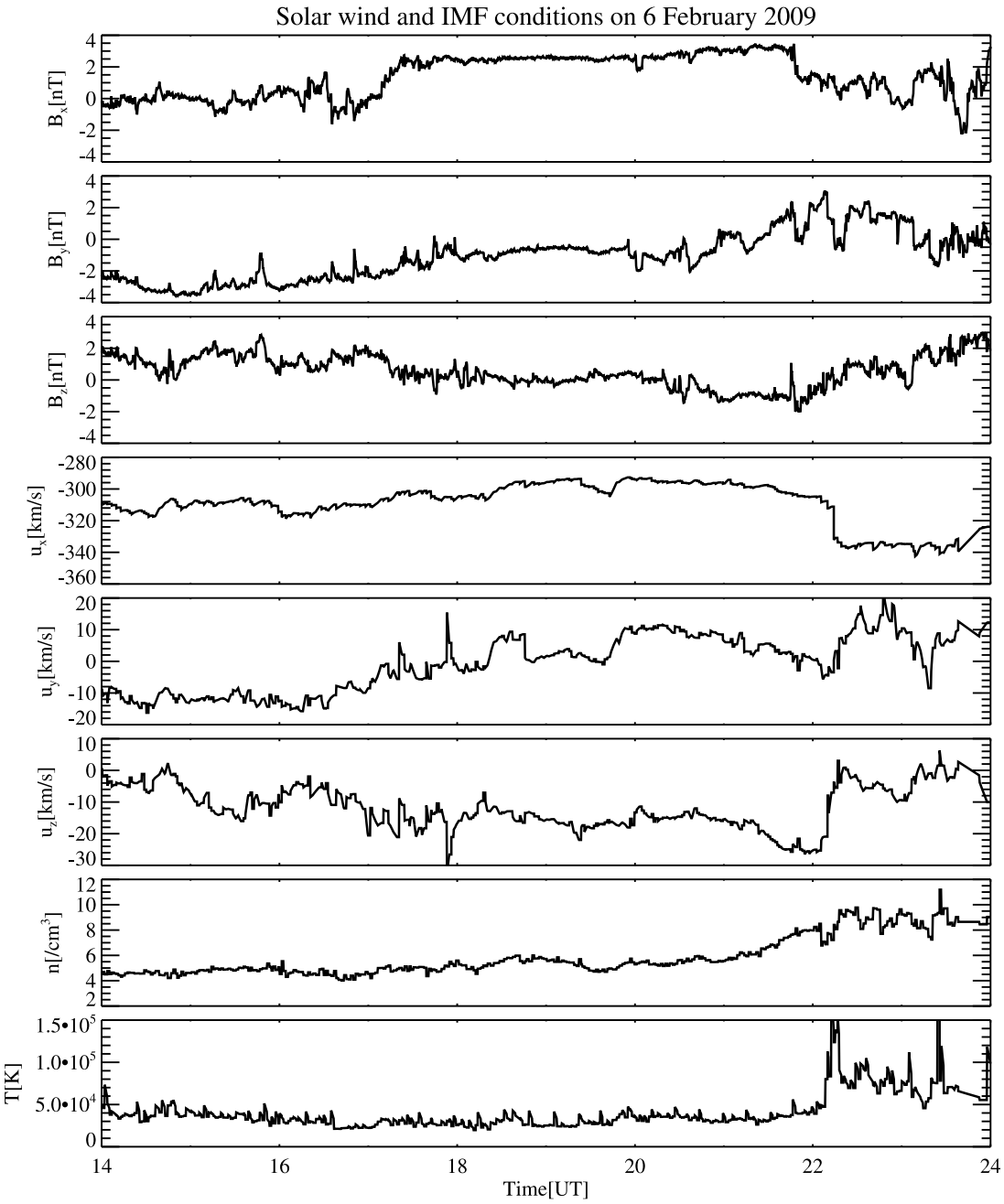

Figure 18. The solar wind and IMF conditions from ACE and WIND data for 12:00–24:00 UT on 6 February 2009.

which does not seem to widen the magnetosheath more for the northward IMF than for the southward IMF.

[48] With northward IMF, a plasma depletion layer just outside of the magnetopause forms. The depletion layer is identified by decreased plasma density and increased magnetic field strength relative to the adjacent magnetosheath plasma [*Zwan and Wolf*, 1976], as marked by the shadowed region in Figure 12. The comparison between the isotropic MHD and the anisotropic MHD with growth-rate based τ, τ = 10 s and τ = 100 s reveals that pressure anisotropy increases the density depletion, although the overall effect is very small. The same conclusion has been drawn by Denton from the study of a 2-D magnetosheath model [*Denton and Lyon*, 2000].

3.2. Quiet Time Magnetosphere

[49] To further validate our model, we perform magnetospheric simulations driven by real solar wind and IMF conditions. As we do not couple any ring current model to anisotropic BATS-R-US for this study, we only simulate the quiet time magnetosphere. Two time periods are selected based on the geomagnetic activity level indicated by the *Dst* index, the positions of the THEMIS satellites and the data avaiability. Both the dayside and nightside magnetosphere

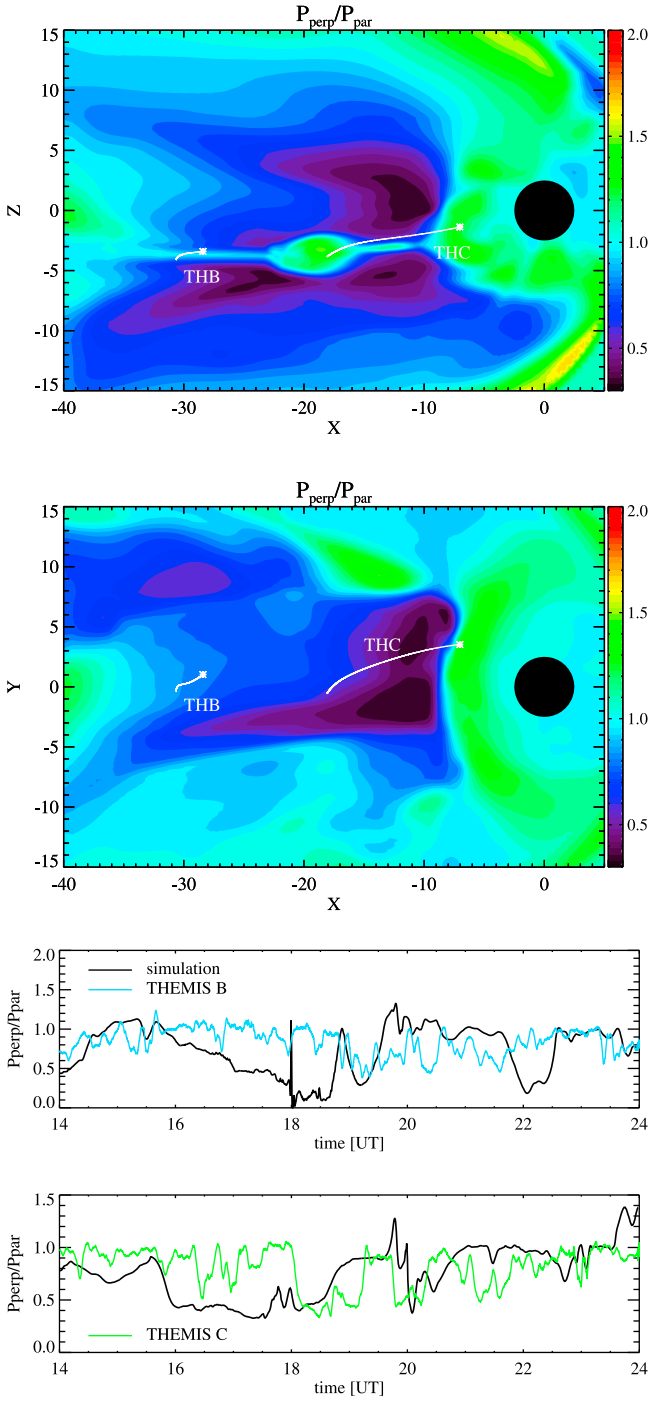

Figure 19. The pressure anisotropy ratio $p_\perp / p_\parallel$ in the $Y = 0$ (top left) and $Z = 0$ (top right) planes at 24:00 UT on 6 February 2009. Trajectories of THEMIS B and C during 14:00–24:00 UT are shown by white lines started from the stars. The two bottom panels show the simulated $p_\perp / p_\parallel$ (black lines) against the actual data along the satellite trajectories.

are covered in our validation. We apply the global relaxation term in the simulations.

3.2.1. Dayside Validation – 16 June 2008

[50] The first time interval we choose is 12:00–24:00 UT on 16 June 2008, when two THEMIS satellites B and C went across the dayside magnetosheath and the bow shock. The solar wind and IMF conditions measured by the ACE satellite are shown in Figure 13. The IMF B_z component varies a bit between positive and negative values, yet the magnitude is small. The average *Dst* index during this period is about −13 nT. Therefore the magnetosphere basically stays in a quiet state.

[51] The 3-D computational domain extends from $X = -224\ R_e$ to $X = 32\ R_e$, from $Y = -128\ R_e$ to $Y = 128\ R_e$, and from $Z = -128\ R_e$ to $Z = 128\ R_e$. To better capture the magnetosheath where THEMIS B and C cross, we increase the grid resolution to $1/8\ R_e$ in that region. Other parameters are the same as they are in the idealized simulations. We perform two simulations with anisotropic and isotropic BATS-R-US respectively. We use the growth-rate based relaxation time and the global relaxation time 200 s in the anisotropic MHD run.

[52] First we look at the pressure anisotropy. In the top panel of Figure 14, we plot the anisotropy ratio $p_\perp / p_\parallel$ at 18:00 UT in the meridional and the equatorial planes, with the trajectories of THEMIS B and C overplotted. The lower two panels show the anisotropy ratio extracted along the satellite orbits from the simulation against the actual data. The comparison indicates that the simulation does fairly well in reproducing the anisotropy ratio in the magnetosheath, including the anisotropy jumps near the magnetopause.

[53] Second, as the idealized simulations show the evidence of the mirror and ion cyclotron instabilities across the magnetosheath, we plot the criteria and relaxation times of these two instabilities along the satellite orbits in Figure 15. The first and third row from top show the variations of the anisotropy factor $A = p_\perp / p_\parallel - 1$ with red lines representing the mirror and ion cyclotron unstable bound respectively. An instability is excited if A is larger than the unstable bound, i.e., the black line is higher than the red one, under which circumstance the relaxation times are shown in the second and fourth row. The mirror and ion cyclotron instabilities are found in the time interval of 13:00–16:50 UT during the magnetosheath crossing by THEMIS B, and in the time interval of 16:50–23:00 UT for THEMIS C. The mirror instability plays a more important role, because its bound is exceeded by approximately the same amount as the ion cyclotron instability bound is exceeded, but the relaxation time of the mirror instability is much smaller than that of the ion cyclotron instability, so the former results in larger changes in the parallel pressure.

[54] Finally, we extract the number density, total pressure, velocity and magnetic field from the anisotropic MHD simulation to compare with the data from the ESA instrument and the isotropic MHD solutions, as shown in Figure 16 and Figure 17. The root-mean-square (RMS) errors with respect to the data are presented in Table 1. Overall the anisotropic and isotropic MHD simulations give very similar variations of the MHD variables across the magnetosheath. The simulations both resemble the measurements reasonably. However, we are more interested in any improvements or drawbacks brought by the anisotropic MHD simulation. One improvement we observe from the figures is that the anisotropic MHD simulation reduces or even eliminates some sudden drops in the density, the total pressure and especially the velocity behind the bow shock, leading to better agreement with the data. The RMS errors reveal an obvious improvement on the velocity. Note both

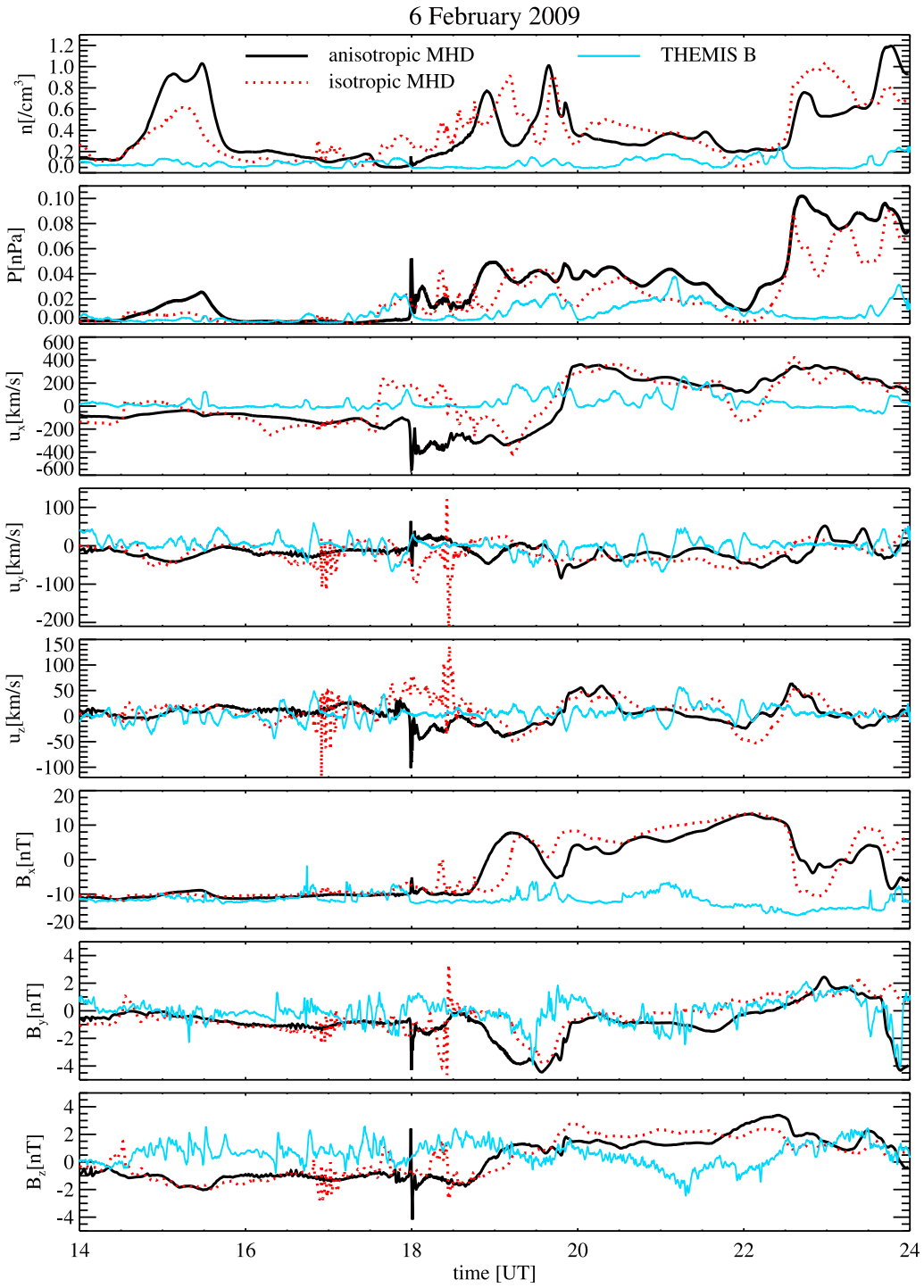

Figure 20. The simulated and measured variables along the THEMIS B orbit during 14:00–24:00 UT on 6 February 2009.

the anisotropic and isotropic MHD simulations do not predict the location of the bowshock well especially for THEMIS C crossing. But the discrepancy between simulated and measured bowshock locations can also be caused by the plane parallel solar wind conditions based on a point measurement by ACE. We checked that the agreement with data is improved if the satellite positions are shifed slightly (by 0.2 R_e) toward the positive X direction.

3.2.2. Nightside Validation – 6 February 2009

[55] The second time interval is 14:00–24:00 UT on 6 February 2009, during which the THEMIS satellites were in the nightside magnetosphere. Both THEMIS B and C were close to the tail current sheet. Figure 18 shows the solar wind and IMF conditions from the combined ACE and WIND data. B_z has small variarions around 0. The averaged *Dst* index is about −14 nT.

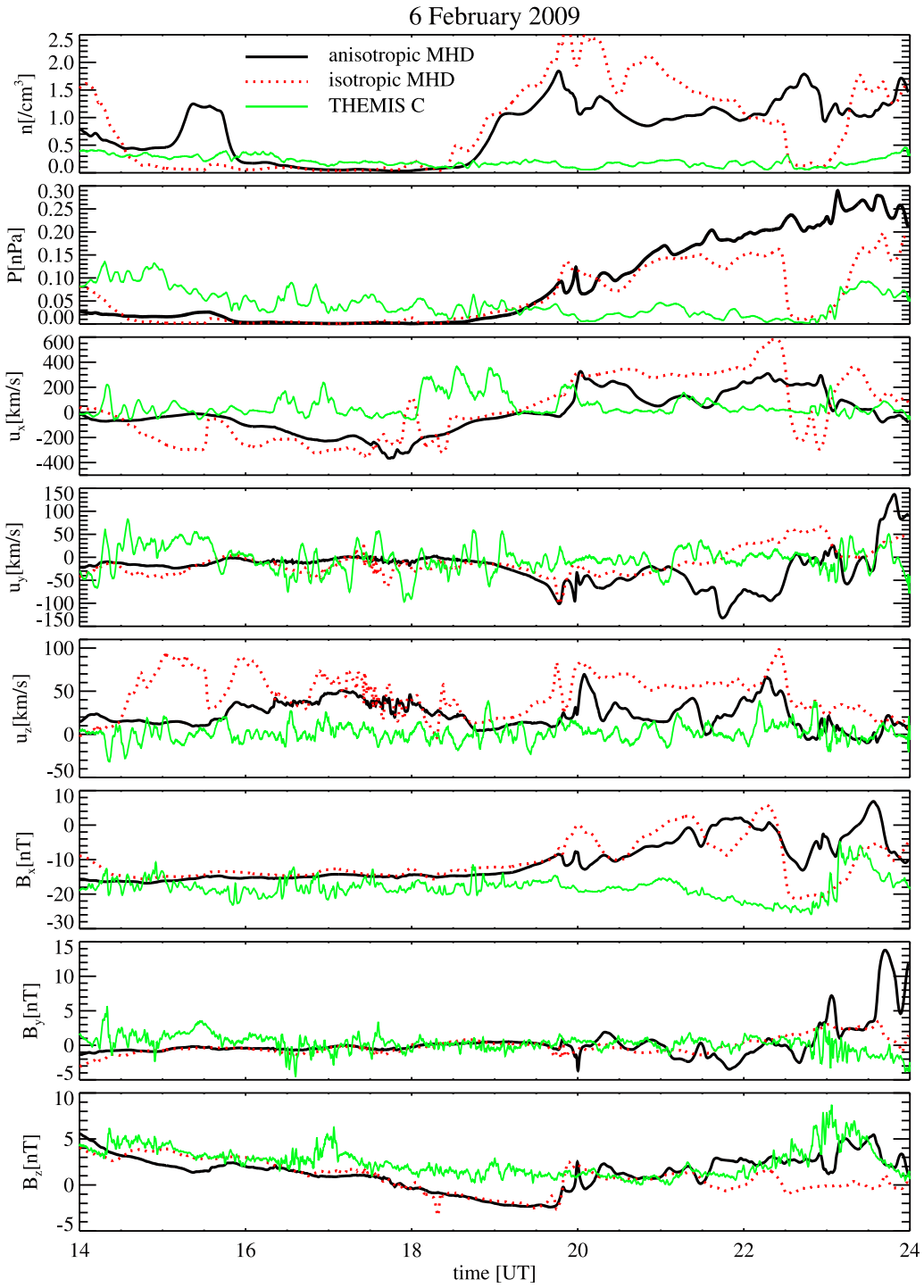

Figure 21. The simulated and measured variables along the THEMIS C orbit during 14:00–24:00 UT on 6 February 2009.

[56] We compute the simulations in a manner similar to the dayside study, except that we do not have a high resolution magnetosheath, but 1/8 R_e resolution in the tail where the satellites cross. Both the anisotropic MHD with growth-rate depended τ and isotropic MHD simulations are conducted.

[57] We plot $p_\perp$ / $p_\parallel$ in the $Y = 0$ and $Z = 0$ planes and overplot the satellite trajectories in the top panels of Figure 19. A direct comparison between the simulation and the data is shown in lower panels. The overall results are much worse than the dayside comparison, as the tail dynamics cannot be fully described by MHD.

[58] The number density, total pressure, velocity and magnetic field profiles along the satellite orbits are shown in Figure 20 and Figure 21. Table 2 shows the RMS errors. The agreement looks poor compared to the dayside case.

Table 2. RMS Errors of the Simulated Variables: 6 February 2009 Event

	THEMIS B		THEMIS C	
	Isotropic MHD	Anisotropic MHD	Isotropic MHD	Anisotropic MHD
n [/cc]	0.39	0.40	1.00	0.78
u_x [km/s]	195.07	222.87	272.14	201.28
u_y [km/s]	40.78	37.39	49.98	59.27
u_z [km/s]	32.89	28.45	53.57	32.07
b_x [nT]	13.37	12.46	10.10	10.10
b_y [nT]	1.30	1.38	1.98	3.11
b_z [nT]	1.93	1.89	2.44	2.04

However, compared to the isotropic simulation, the anisotropic MHD simulation improves the agreement with data on u_y and u_z for THEMIS B and u_x and u_z for THEMIS C. This matches with the results we have seen in the idealized simulations, as the anisotropic MHD model reduces the plasma speed in the tail. But the u_x agreement is worse in the anisotropic case for THEMIS B. The anisotropic MHD simulation also sightly improves the magnetic field agreement with the data, particularly B_z for THEMIS C. Note a major contradiction to the measurement occurs at around 19:00 UT, when both the isotropic and anisotropic MHD simulations predict that THEMIS B crosses the current sheet, identified by the sign change of B_x. The incorrect position of the simulated current sheet closely relates to the bad data-model agreement on other variables.

4. Conclusions

[59] We have implemented the anisotropic MHD equations into the BATS-R-US MHD model to take into account the effects of pressure anisotropy in space plasmas. The anisotropic MHD equation set differs from the isotropic MHD equation set in the momentum, pressure and energy equations. The pressure equations follow the double adiabatic approximation. As anisotropic MHD does not contain sufficient jump conditions across a discontinuity, we supplement the conservation laws with bounded pressure anisotropy provided by the firehose, mirror and ion cyclotron instabilities. The instability criteria are also applied to limit the pressure anisotropy wherever the plasma becomes unstable through the pressure relaxation term that reduces pressure anisotropy in a given relaxation time τ. We implement two options for setting τ. One is a constant and uniform value, the other is based on the instability growth rates, which in turn depend on local plasma parameters. In addition, we have the global relaxation term that limits the pressure anisotropy everywhere.

[60] To validate the model, we have performed 3-D global magnetospheric simulations with anisotropic BATS-R-US. The idealized magnetosphere simulations with southward IMF show several interesting differences between anisotropic and isotropic MHD in modeling the magnetosphere, further revealing the effects of pressure anisotropy. First of all, pressure anisotropy thickens the magnetosheath and changes the shape of the magnetosphere. Second, pressure anisotropy reduces the reconnection rate and consequently the flow speed in the tail significantly. Third, pressure anisotropy increases the nightside plasma pressure and forms a pressure peak away from the Earth. The increase in the nightside pressure strengthens the region 2 currents. The steepened pressure distribution results in a stronger ring current. Some of these results are supported by previous studies that obtained similar features. The idealized magnetosphere simulations with northward IMF confirms the increased density depletion near the magnetopause resulting from pressure anisotropy that has been found by past studies.

[61] The simulations of the quiet time magnetosphere provides a direct evaluation of the anisotropic MHD model when comparing the simulations to the measurements. In general the model predicts the dayside magnetosheath better than the nightside magnetosphere. Compared to the isotropic MHD simulations, the anisotropic MHD simulations improve the model-data agreement on the velocity most. Not much improvement has been seen in the other variables.

[62] Despite of its many advantages, our anisotropic MHD model exhibits several limitations that may require improvements in the future. First of all, the anisotropic pressure equations are formulated equivalently to the double adiabatic equations. However, the double adiabatic approximation is not applicable to some processes, for example mirror instability [*Kulsrud*, 1982; *Shi et al.*, 1987]. Although the pressure relaxation term mimics the effect of instabilities on pressure, it is still an approximation. Second, like isotropic MHD, anisotropic MHD based on the double adiabatic approximation is not appropriate to describe the inner magnetospheric dynamics, since it cannot capture the diamagnetic drift and neglects the heat flux [*Wolf et al.*, 2009; *Heinemann and Wolf*, 2001]. To better describe the near-Earth plasma and perform geomagnetic storm simulations, we couple the anisotropic BATS-R-US model to inner magnetospheric models that capture various kinetic processes. The details will be reported in a follow-up paper.

[63] **Acknowledgments.** The authors thank Margaret G. Kivelson for valuable discussions on mirror and ion cyclotron instabilities. The authors acknowledge N. Ness at Bartol Research Institute, D. J. McComas at SWRI, K. Ogilvie at NASA GSFC and CDAWeb for providing the IMF and solar wind data from ACE and WIND. This work was supported by various research grants from NASA and NSF. Computing resources were provided by the NASA High-End Computing (HEC) Program through the NASA Advanced Supercomputing (NAS) Division at Ames Research Center.

[64] Masaki Fujimoto thanks You-Qiu Hu and another reviewer for their assistance in evaluating this paper.

References

Abraham-Shrauner, B. (1967), Shock jump conditions for an anisotropic plasma, *J. Plasma Phys.*, *1*(3), 379–381.

Anderson, D. N., D. T. Decker, and C. E. Valladares (1996), Modeling boundary blobs using time-varying convection, *Geophys. Res. Lett.*, *23*(5), 579, doi:10.1029/96GL00371.

Angelopoulos, V., et al. (1994), Statistical characteristics of bursty bulk flow events, *J. Geophys. Res.*, *99*(A11), 21,257–21,280, doi:10.1029/94JA01263.

Baranov, V. B. (1970), Simple waves in a plasma with anisotropic pressure, *Fluid Dyn.*, *5*(2), 181–186.

Barnes, A. (1966), Collisionless damping of hydromagnetic waves, *Phys. Fluids*, *9*(8), 1483–1495, doi:10.1063/1.1761882.

Baumjohann, W., and G. Pashmann (1989), Average plasma properties in the central plasma sheet, *J. Geophys. Res.*, *94*(A6), 6597–6606, doi:10.1029/JA094iA06p06597.

Birn, J., et al. (2001), Geospace Environmental Modeling (GEM) magnetic reconnection challenge, *J. Geophys. Res.*, *106*(A3), 3715–3720, doi:10.1029/1999JA900449.

Boris, J. P. (1970), A physically motivated solution of the Alfvén problem, *NRL Tech. Rep. 2167*, Nav. Res. Lab., Washington, D. C.

Chandrasekhar, S., A. N. Kaufman, and K. M. Watson (1958), The stability of the pinch, *Proc. R. Soc. London, Ser. A*, *245*, 435–455.

Chao, J. K., and B. Goldstein (1972), Modification of the Rankine-Hugoniot relations for shocks in space, *J. Geophys. Res.*, *77*(28), 5455–5466, doi:10.1029/JA077i028p05455.

Cheng, C. Z. (1992), Magnetospheric equilibrium with anisotropic pressure, *J. Geophys. Res.*, *97*(A2), 1497–1510, doi:10.1029/91JA02433.

Chew, G. F., M. L. Goldberger, and F. E. Low (1956), The Boltzmann equation and the one-fluid hydromagnetic equations in the absence of particle collisions, *Proc. R. Soc. London, Ser. A*, *236*, 112–118.

Denton, R. E., and J. G. Lyon (2000), Effect of pressure anisotropy on the structure of a two-dimensional magnetosheath, *J. Geophys. Res.*, *105*(A4), 7545–7556, doi:10.1029/1999JA000360.

Denton, R. E., B. J. Anderson, S. P. Gary, and S. A. Fuselier (1994), Bounded anisotropy fluid model for ion temperatures, *J. Geophys. Res.*, *99*(A6), 11,225–11,241, doi:10.1029/95JA00656.

Erkaev, N. V., C. J. Farrugia, and H. K. Biernat (1999), Three-dimensional, one-fluid, ideal MHD model of magnetosheath flow with anisotropic pressure, *J. Geophys. Res.*, *104*(A4), 6877–6887, doi:10.1029/1998JA900134.

Erkaev, N. V., D. F. Vogl, and H. K. Biernat (2000), Solution for jump conditions at fast shocks in an anisotropic magnetized plasma, *J. Plasma Phys.*, *64*(5), 561–578, doi:10.1017/S002237780000893X.

Fok, M.-C., R. A. Wolf, R. W. Spiro, and T. E. Moore (2001), Comprehensive computational model of Earth's ring current, *J. Geophys. Res.*, *106*(A5), 8417–8424, doi:10.1029/2000JA000235.

Gary, J. B., R. A. Heelis, and J. P. Thayer (1995), Summary of field-aligned Poynting flux observations from DE 2, *Geophys. Res. Lett.*, *22*(14), 1861–1864, doi:10.1029/95GL00570.

Gary, S. P. (1992), The mirror and ion-cyclotron anisotropy instabilities, *J. Geophys. Res.*, *97*(A6), 8519–8529, doi:10.1029/92JA00299.

Gary, S. P., M. D. Montgomery, W. C. Feldman, and D. W. Forslund (1976), Proton temperature anisotropy instabilities in the solar wind, *J. Geophys. Res.*, *81*(7), 1241–1246, doi:10.1029/JA081i007p01241.

Gary, S. P., M. E. McKean, and D. Winske (1993), Ion cyclotron anisotropy instabilities in the magnetosheath: Theory and simulations, *J. Geophys. Res.*, *98*(A3), 3963–3971, doi:10.1029/92JA02585.

Gary, S. P., M. E. McKean, D. Winske, B. J. Anderson, R. E. Denton, and S. A. Fuselier (1994), The proton cyclotron instability and the anisotropy/β inverse correlation, *J. Geophys. Res.*, *99*(A4), 5903–5914, doi:10.1029/93JA03583.

Gary, S. P., H. Li, S. O'Rourke, and D. Winske (1998), Proton resonant firehose instability: Temperature anisotropy and fluctuating field constraints, *J. Geophys. Res.*, *103*(A7), 14,567–14,574, doi:10.1029/98JA01174.

Hall, A. N. (1979), Finite ion Larmor radius modifications to the firehose and mirror instabilities, *J. Plasma Phys.*, *21*, 431–443.

Hall, A. N. (1980), On the origin of long time-scale pulsar scintillations: II. Growth of the mirror instability, and non-linear amplitude limitation, *Mon. Not. R. Astron. Soc.*, *190*, 371–383.

Hall, A. N. (1981), The firehose instability in interstellar space, *Mon. Not. R. Astron. Soc.*, *195*, 685–696.

Heinemann, M., and R. A. Wolf (2001), Relationships of models of the inner magnetosphere to the Rice Convection Model, *J. Geophys. Res.*, *106*(A8), 15,545–15,554, doi:10.1029/2000JA000389.

Hesse, M., and J. Birn (1992), MHD modeling of magneototail instability for anisotropic pressure, *J. Geophys. Res.*, *97*(A7), 10,643–10,654, doi:10.1029/92JA00793.

Horton, W., L. Cheung, J.-Y. Kim, and T. Tajima (1993), Self-consisent plasma pressure tensors from the Tsyganenko magnetic field models, *J. Geophys. Res.*, *98*(A10), 17,327–17,343, doi:10.1029/93JA00794.

Hudson, P. D. (1970), Discontinuities in an anisotropic plasma and their identification in the solar wind, *Planet. Space Sci.*, *18*, 1611–1622.

Kennel, C. F., and H. E. Petschek (1966), Limit on stably trapped particle fluxes, *J. Geophys. Res.*, *71*(1), 1–28, doi:10.1029/JZ071i001p00001.

Koren, B. (1993), A robust upwind discretization method for advection, diffusion and source terms, in *Numerical Methods for Advection-Diffusion Problems*, edited by C. Vreugdenhil and B. Koren, pp. 117–138, Vieweg, Braunschweig, Germany.

Kulsrud, R. M. (1982), MHD description of plasma, in *Handbook of Plasma Physics Volume I: Basic Plasma Physics 1*, edited by A. A. Galeev and R. N. Sudan, pp. 115–145, North-Holland, Amsterdam.

Lazar, M., and S. Poedts (2009a), Limits for the firehose instability in space plasmas, *Sol. Phys.*, *258*(1), 119–128.

Lazar, M., and S. Poedts (2009b), Firehose instability in space plasmas with bi-kappa distributions, *Astron. Astrophys.*, *494*(1), 311–315.

Lui, A. T. Y., and D. C. Hamilton (1992), Radial profiles of quiet time magnetospheric parameters, *J. Geophys. Res.*, *97*(A12), 19,325–19,332, doi:10.1029/92JA01539.

Lui, A. T. Y., H. E. Spence, and D. P. Stern (1994), Empirical modeling of the quiet time nightside magnetosphere, *J. Geophys. Res.*, *99*(A1), 151–157, doi:10.1029/93JA02647.

Lynn, Y. M. (1967), Discontinuities in an anisotropic plasma, *Phys. Fluids*, *10*, 2278–2280, doi:10.1063/1.1762025.

Lyu, L. H., and J. R. Kan (1986), Shock jump conditions modified by pressure anisotropy and heat flux for earth's bowshock, *J. Geophys. Res.*, *91*(A6), 6771–6775, doi:10.1029/JA091iA06p06771.

Märk, E. (1974), Growth rates of the ion cyclotron instability in the magnetosphere, *J. Geophys. Res.*, *79*(22), 3218–3220, doi:10.1029/JA079i022p03218.

Meng, X., G. Tóth, I. V. Sokolov, and T. I. Gombosi (2012), Classical and semirelativistic magnetohydrodynamics with anisotropic ion pressure, *J. Comput. Phys.*, *231*, 3610–3622, doi:10.1016/j.jcp.2011.12.042.

Neubauer, F. (1970), Jump relations for shocks in an anisotropic plasma, *Z. Physik*, *237*, 205–223.

Phan, T.-D., G. Paschmann, W. Baumjohann, N. Sckopke, and H. Lühr (1994), The magnetosheath region adjacent to the dayside magnetopause: AMPTE/IRM observations, *J. Geophys. Res.*, *99*(A1), 121–141, doi:10.1029/93JA02444.

Pokhotelov, O. A., R. Z. Sagdeev, M. A. Balikhin, and R. A. Treumann (2004), Mirror instability at finite ion-Larmor radius wavelengths, *J. Geophys. Res.*, *109*, A09213, doi:10.1029/2004JA010568.

Powell, K. G., P. L. Roe, T. J. Linde, T. I. Gombosi, and D. L. De Zeeuw (1999), A solution-adaptive upwind scheme for ideal magnetohydrodynamics, *J. Comput. Phys.*, *154*, 284–309, doi:10.1006/jcph.1999.6299.

Ridley, A., T. I. Gombosi, and D. L. De Zeeuw (2004), Ionospheric control of the magnetosphere: Conductance, *Ann. Geophys.*, *22*, 567–584.

Samsonov, A. A., and M. I. Pudovkin (2000), Application of the bounded anisotropy model for the dayside magnetosheath, *J. Geophys. Res.*, *105*(A6), 12,859–12,867, doi:10.1029/2000JA900009.

Samsonov, A. A., O. Alexandrova, C. Lacombe, M. Maksimovic, and S. P. Gary (2007), Proton temperature anisotropy in the magnetosheath: Comparison of 3-D MHD modelling with cluster data, *Ann. Geophys.*, *25*, 1157.

Shi, Y., L. C. Lee, and Z. F. Fu (1987), A study of tearing instability in the presence of a pressure anisotropy, *J. Geophys. Res.*, *92*(A11), 12,171–12,179, doi:10.1029/JA092iA11p12171.

Shoji, M., Y. Omura, B. T. Tsurutani, O. P. Verkhoglyadova, and B. Lembege (2009), Mirror instability and L-mode electromagnetic ion cyclotron instability: Competition in the Earth's magnetosheath, *J. Geophys. Res.*, *114*, A10203, doi:10.1029/2008JA014038.

Sokolov, I. V., E. V. Timofeev, J. ichi Sakai, and K. Takayama (2002), Artificial wind—A new framework to construct simple and efficient upwind shock-capturing schemes, *J. Comput. Phys.*, *181*, 354–393, doi:10.1006/jcph.2002.7130.

Southwood, D. J., and M. G. Kivelson (1993), Mirror instability: 1. Physical mechanism of linear instability, *J. Geophys. Res.*, *98*(A6), 9181–9187, doi:10.1029/92JA02837.

Tajiri, M. (1967), Propagation of hydromagnetic waves in collisionless plasma: II. Kinetic approach, *J. Phys. Soc. Japan*, *22*(6), 1482–1494.

Tóth, G., et al. (2012), Adaptive numerical algorithms in space weather modeling, *J. Comput. Phys.*, *231*, 870–903, doi:10.1016/j.jcp.2011.02.006.

Vogl, D. F., H. K. Biernat, N. V. Erkaev, C. J. Farrugia, and S. Mühlbachler (2001a), Jump conditions for pressure anisotropy and comparison with the earth's bow shock, *Nonlinear Processes Geophys.*, *8*(3), 167–174.

Vogl, D. F., N. V. Erkaev, H. K. Biernat, S. Mühlbachler, and C. J. Farrugia (2001b), Jump conditions at fast shocks in an anisotropic magnetized plasma, *Adv. Space Res.*, *28*(6), 851–856, doi:10.1016/S0273-1177(01)00503-8.

Wolf, R. A., Y. Wan, X. Xing, J.-C. Zhang, and S. Sazykin (2009), Entropy and plasma sheet transport, *J. Geophys. Res.*, *114*, A00D05, doi:10.1029/2009JA014044.

Wu, L., F. Toffoletto, R. A. Wolf, and C. Lemon (2009), Computing magnetospheric equilibria with anisotropic pressures, *J. Geophys. Res.*, *114*, A05213, doi:10.1029/2008JA013556.

Zaharia, S., C. Z. Cheng, and K. Maezawa (2004), 3-D force-balanced magnetospheric configurations, *Ann. Geophys.*, *22*, 251–266.

Zwan, B. J., and R. A. Wolf (1976), Depletion of solar wind plasma near a planetary boundary, *J. Geophys. Res.*, *81*(10), 1636–1648, doi:10.1029/JA081i010p01636.